ALMA MATER STUDIORUM
UNIVERSITÀ DI BOLOGNA

Master's degree in Electrical Engineering
"Guglielmo Marconi" Department of Electrical, Electronic and Information Engineering DEI

EXPLORING THE PIEZOELECTRIC BEHAVIOR OF MELTBLOWN POLYMER NONWOVENS FOR THE DEVELOPMENT OF POLYMERIC FIBERS IN ENERGY HARVESTING AND SENSING

Master's thesis in Innovative Electrical Technologies

Supervisor

Prof. Fabiani Davide

Presented by

Rocchetti Giacomo

Co-Supervisors

Prof. Dr. Rychkov Dmitry

Gasperini Leonardo

Academic year 2025/2026

Graduation session V

INDEX

ABSTRACT

This thesis investigates the piezoelectric behaviour and thermal stability of melt-blown polypropylene (PP) nonwoven ferroelectrets—a format not yet comprehensively characterised in the literature. As-received PP nonwovens and PP nonwovens produced from a blend containing 30 wt% of H_3PO_4-treated pellets were studied through two Designs of Experiments (DoEs) and compared with existing results for other ferroelectret polymers.

In DoE 1 (process-factor screening), a full factorial design (2 × 4 × 3, 72 tests) quantified the effect of phosphorus treatment (P), intermediate layers (N), and charging voltage (V) on d_{33} through ANOVA. The phosphorus treatment is the dominant factor (43.7% of total variation, $p < 0.001$), followed by voltage (13.9%, $p < 0.001$), with a significant P × V interaction. In DoE 2, thermally stimulated charge decay (TSCD) and temperature-dependent d_{33} measurements were carried out for the optimal configurations identified in DoE 1.

The results show that as-received PP nonwovens exhibit a d_{33} approximately 3–4 times higher than their H_3PO_4-treated counterparts (~108–130 pC/N vs. ~30 pC/N at room temperature), while treated samples demonstrate improved relative thermal stability. Notably, H_3PO_4 treatment has the opposite effect on d_{33} in PP nonwovens (−70%) compared to LDPE (+50%), attributed to the pre-extrusion application altering fibre morphology rather than solely modifying surface trap properties. This work ranks in the middle range among ferroelectret polymers in the literature, with a remarkable d_{33} for a non-optimised format but limited thermal stability. The sensitivity/stability trade-off, identified in the literature as "the central engineering challenge", is confirmed and quantified for the first time in the nonwoven format.

1. INTRODUCTION

1.1 Scientific and technological background

The rapid expansion of the Internet of Things (IoT) and wearable electronics is creating an ever-growing demand for sensing nodes that are lightweight, distributed, and capable of autonomous operation [2, pp. 1–2] [4, pp. 1–2]. Conventional batteries, while practical, impose constraints of limited energy density, periodic replacement, and environmental end-of-life concerns that become especially problematic in body-worn and remote-access applications [2, p. 2] [4, p. 2]. In this context, piezoelectric energy harvesting—the direct conversion of ambient or biomechanical mechanical energy into electricity—offers a compelling route to self-powered, maintenance-lean operation for the low-power devices (typically 100 µW to 1 mW) that underpin modern sensor networks [2, p. 8] [4, p. 2].

Ceramic piezoelectrics such as lead zirconate titanate (PZT, pC/N) remain the performance benchmark, but their brittleness, high density, and lead content limit their suitability for flexible, wearable, and large-area formats [1, p. 67; 3, p. 1]. Piezoelectric polymers address these limitations through mechanical compliance, low density, and straightforward processability into films, fibres, and nonwovens [1, p. 67; 3, p. 12]. Three main families have emerged: **(i)** intrinsic piezoelectric polymers, led by poly(vinylidene fluoride) (PVDF) and its copolymers, whose response originates from molecular dipole alignment; **(ii)** polymer–ceramic composites, which combine a flexible matrix with a high-d filler; **(iii)** ferroelectrets (piezoelectrets), cellular or voided polymer structures in which electric charges trapped on the internal surfaces of gas-filled cavities form deformable macroscopic dipoles [1, pp. 69–70] [3, p. 12].

Among ferroelectret materials, polypropylene (PP) is the most widely studied: commercially available cellular PP films have demonstrated values exceeding 600 pC/N, surpassing PVDF by more than an order of magnitude [3, p. 19]. Melt-blowing is a scalable industrial process that produces nonwoven mats composed of ultrafine fibres (µm), yielding a highly porous microstructure with a large surface-to-volume ratio—an architecture intrinsically suited to ferroelectret functionality. The present thesis investigates the piezoelectric behaviour of melt-blown PP nonwovens, with all experimental activities carried out at the Technology and Study Centre (TSC) in Weißenburg, which provides an integrated workflow from fibre production to multimodal characterisation.

1.2 Research motivation and relevance

Despite their outstanding piezoelectric coefficients, PP-based ferroelectrets suffer from a well-documented limitation: the trapped charge, and consequently the piezoelectric coefficient, begins to decay at temperatures as low as 60 °C due to the relatively shallow trap states characteristic of polypropylene [1, p. 74]. This thermal ceiling constrains the use of PP ferroelectrets in environments where even moderate heating occurs—including proximity to the human body (37 °C at the skin) and exposure to direct sunlight or warm indoor conditions [4, p. 21].

Recent work has shown that chemical treatments of the polymer prior to processing—such as orthophosphoric acid (H_3PO_4) for PP and low-density polyethylene, or titanium tetrachloride ($TiCl_4$) vapour for fluorinated ethylene propylene—can deepen the trap-energy spectrum and shift the onset of charge decay upward by 40–60 °C. However, these findings have been demonstrated primarily on thin films and tubular-channel ferroelectrets; systematic data on the piezoelectric response and its thermal stability in melt-blown PP nonwovens are lacking. In parallel, the dependence of wearable and distributed IoT systems on rechargeable batteries remains a bottleneck for truly autonomous operation [2, p. 2] [4, p. 2]. Piezoelectric nonwovens based on PP could offer a route towards self-powered textile-grade sensors and energy harvesters, provided that the thermal stability of the charge can be understood and controlled. Addressing this gap would contribute to extending the operational window of PP ferroelectrets, providing reference data for the design of nonwoven-based piezoelectric devices, and reducing the maintenance burden of distributed sensing systems [2, p. 8] [3, p. 20] [4, p. 23].

1.3 Objectives of the thesis

As mentioned above, the objective of this thesis is to establish a direct link between the thermal stability and the macroscopic piezoelectric performance of polypropylene nonwovens, contributing to the broaded effort of developing thermally stable, lightweight, and fully polymeric piezoelectric materials.

To pursue this objective, the following experimental activities are carried out:

1. Produce melt-blown nonwoven mats from both untreated PP and blends containing 30 wt% of orthophosphoric acid (H_3PO_4)-treated pellets, to assess the effect of chemical treatment on the resulting fibre morphology and electret properties.
2. Corona-charge the nonwoven samples and measure their piezoelectric coefficient as a function of temperature to quantify the thermal stability of the piezoelectric response.

3. Perform thermally stimulated charge decay (TSCD) measurements and understand temperature dependence of piezoelectric coefficient, to characterise the materials and correlate it with the macroscopic behaviour.
4. Compare the results for treated and untreated samples to evaluate whether the treatment provides a measurable improvement in charge retention and piezoelectric stability for the melt-blown nonwoven format.

1.4 Structure of the document

This thesis is organised into the following chapters:

- **Chapter 1** (the present chapter) provides the scientific and technological background, the research motivation, the objectives, and the document structure.
- **Chapter 2—State of the Art** reviews the relevant literature in three blocks: polymeric materials and their processing, including melt-blowing (**Section 2.1**); charge injection, transport, and trapping mechanisms in polymer dielectrics, together with strategies to improve charge stability (**Section 2.2**); and the fundamentals of piezoelectricity and the routes by which polymers—and PP in particular—acquire piezoelectric properties (**Section 2.3**);
- **Chapter 3—Methodology and Research Activities** describe the material selection, the melt-blowing process, and the experimental techniques for morphological, structural, thermal, mechanical, and electrical characterisation.
- **Chapter 4—Experimental Results** presents the outcomes of the analyses, including fibre morphology, thermal and mechanical performance, corona charging, TSCD, and as a function of temperature.
- **Chapter 5—Discussion** interprets the results in the context of the existing literature, highlighting strengths, limitations, and potential improvements.
- **Chapter 6—Conclusions** summarise the findings and their broader significance.
- **Chapter 7—References** complete the document.

2. STATE OF THE ART

This chapter is dedicated to exploring the state of the art related to: **(i)** reviews of functional polymers and how they are manufactured; **(ii)** analysis of the main conduction mechanisms in polymeric materials; **(iii)** properties of piezoelectricity and how it is applied to polymers.

2.1 Functional polymeric materials

2.1.1 Types of polymeric materials

Chemical Foundations and Molecular Structure. Polymeric materials are extensively employed as insulators in both low- and high-voltage electrical equipment, due to their excellent dielectric characteristics, thermal stability, ease of processing, and low cost [6, p. 2]. A polymer is a macromolecule built by the repetition of a basic structural unit (mer), derived from a low-molecular-weight molecule called monomer [5, p. 42]. In addition, polymerisation the monomer is typically unsaturated (carbon–carbon double bond, C=C); during polymerisation this bond opens, yielding a saturated backbone where the structural uniti s chemically identical to the starting monomer [5, pp. 82, 114].

Taking polypropylene (PP) as a main reference to describe polymers' properties, it illustrates this principle: the propylene monomer (CH_2=CH–CH_3) converts into the repeating unit –CH_2–$CH(CH_3)$– [5, p. 115] [6, p. 7]. The chain length is expressed by the degree of polymerisation (DP, number of mers), and the molecular weight ($MW = DP \times MW_{mer}$) [5, pp. 46, 48]. Commercial polymers exhibit a molecular weight distribution characterised by averages M_n (numerical average molecular weight) and M_w (weight average molecular weight) [5, pp. 49–50]; mechanical strength increases with MW up to an asymptotic value, whereas melt viscosity rises continuously, creating a performance–processability trade-off [5, pp. 223, 226].

Stereochemistry and Crystalline Morphology. Stereoisomerism arises when a backbone carbon bears different substituents, allowing three spatial configurations: isotactic (substituents on the same side), syndiotactic (alternating), and atactic (random) [5, pp. 216–217]. Only stereoregular forms can crystallise; atactic polymers (e.g. atactic PS, PMMA) remain amorphous [5, p. 243].

This is critical for polypropylene: industrially, isotactic PP (iPP) is produced via Ziegler–Natta or metallocene catalysts to enable crystallisation [6, p. 7] [7, p. 2]. The crystalline phase of iPP exists in three polymorphs—monoclinic α, trigonal β, and orthorhombic γ—with β-crystal modification yielding simultaneously higher impact strength (+25%) and DC breakdown strength (+10–29%) relative to the α-form [7, pp. 1, 8–9].

Semicrystalline polymers consist of ordered crystallites embedded in an amorphous matrix [5, pp. 240–241]. The crystalline building blocks are chain-folded lamellae that aggregate into spherulites, recognisable under polarised-light microscopy by the “Maltese cross” pattern [5, pp. 271, 276–277] [7, p. 5].

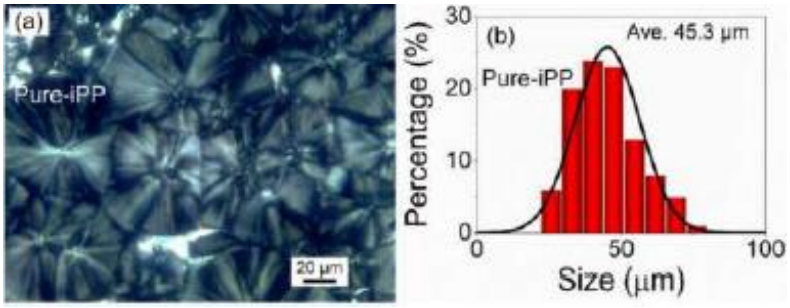

Figure 2.1. *Polarised optical micrograph of spherulites in unfilled isotactic polypropylene. Average diameter ≈ 45 µm. The “Maltese cross” pattern reflects the radial lamellar arrangement. Taken from [7, p. 5, Fig. 1 a–b].*

Thermal Transitions and Dielectric Properties. The chemical constitution of the polymer chain—shape and polarity of the substituents—governs thermal parameters (melting, processing, and service temperatures) as well as electrical behaviour [6, p. 2]. The relative permittivity (ε_r) of commercial polymers ranges from ≈ 2 to 5 (e.g. iPP: 2.28; PVDF: up to 10.5), while the dielectric breakdown strength (BDS) typically falls between 100 and 300 kV/cm for pure plastics, reaching 700 kV/cm for halogenated polymers such as PTFE [6, pp. 2, 14]. For PP an average BDS of 55 kV/cm has been reported, improvable through blending with polyethylene (PE) [6, p. 7].

The degree of crystallinity (fraction of crystalline phase) governs thermal and mechanical response: highly crystalline polymers exhibit a sharp melting temperature (T_m), whereas amorphous polymers show a glass transition (T_g) from glassy to rubbery behaviour; semicrystalline materials display both transitions [5, pp. 300–301]. **Table 2.1** compiles T_g, T_m, ε_r, and BDS for polymers relevant to this work. For iPP (T_g ≈ −10 °C, T_m ≈ 165 °C), room temperature lies well above T_g, which explains the material’s flexibility despite its semicrystalline nature [5, p. 325] [7, p. 2]. Polarised optical microscopy of unfilled iPP reveals spherulites of ≈ 45 µm average diameter, reducible to 2.5–7.6 µm by nucleating agents [7, p. 5].

Table 2.1. *Transition temperatures and dielectric properties of selected polymers. Data compiled from [5, 6, 7]. The PP row is highlighted as the material investigated in this thesis.*

Polymer	Tg (°C)	Tm (°C)	ε_r	BDS (kV/mm)
PP (isotactic)	**–10**	**165–174**	**2.28**	**55**

Polymer	Tg (°C)	Tm (°C)	ε_r	BDS (kV/mm)
PE (HDPE)	–120	127–135	2.3	70
PE (LDPE)	–120	98–120	2.3	79
PET	80	265	3.3	—
PA66	60	265	—	—
PVDF	—	~170	4.09–10.5	—

Classification and Modification of Polymers. From a structural viewpoint, linear and branched chains characterise thermoplastics (separable upon heating), while cross-linked networks define thermosets (non-separable) [5, pp. 60–61, 87] [6, pp. 3–4]. Properties can be tailored via additives: fillers (Al_2O_3, SiO_2, TiO_2, carbon nanotubes, graphene) form nanocomposites with enhanced electrical and mechanical performance [6, pp. 2, 13], and nucleating agents such as β-NA in iPP simultaneously improve toughness and dielectric strength [7, pp. 1, 11].

Based on the above, engineering polymers are grouped into three categories. Thermoplastic polymers are linear or branched macromolecules whose softening upon heating is fully reversible, permitting recycling [6, p. 3]. They include amorphous types (polycarbonate, PMMA) and semicrystalline types such as HDPE and iPP; the latter has attracted interest as a recyclable, non-cross-linking candidate to replace XLPE in high-voltage cable insulation [6, p. 20] [7, p. 2]. Thermosetting polymers feature a covalently cross-linked network that cannot be re-melted; they exhibit T_g but no T_m, and are cured either at ambient temperature or by heating. Common thermosets for electrical applications include epoxy resins, phenol-formaldehyde, and alkyd resins [6, p. 4]. Elastomers are lightly cross-linked polymers capable of large, reversible deformation driven by entropy recovery. Thermoplastic elastomers such as PDMS, EVA, and EPDM are increasingly used as high-voltage insulators owing to their flexibility and weathering resistance [6, pp. 4–5].

Material Selection: Polypropylene (iPP). The choice of polymer type, together with its chemical constitution, tacticity, and crystallinity, determines both the available processing routes and the achievable functional properties. Isotactic polypropylene combines favourable dielectric behaviour, a semicrystalline morphology amenable to charge trapping [7, pp. 1, 11], and excellent processability via melt-based techniques—making it the material of choice for the present thesis. The following section discusses the principal processing techniques for polymeric fibres and structures, with particular emphasis on melt-blowing.

2.1.2 Processing techniques

Comparative opening. The functional properties of a polymeric product depend not only on the choice of material, as discussed in the previous section, but also on the processing route employed to shape it into its final form. For fibre-based structures intended for filtration, sensing, or energy-harvesting applications, several competing techniques exist, each characterised by distinct trade-offs in terms of productivity, morphological control (fibre diameter, porosity), sustainability, and pressure drop (ΔP) across the resulting medium [8, pp. 140S–142S] [11, pp. 1–2]. This section reviews three families of techniques relevant to the present thesis: melt-blowing (MB), which is the technique employed to produce the PP nonwoven samples investigated in this thesis; solution blow spinning (SBS) and its hybrid variants; and extrusion-based additive manufacturing (AM).

Melt-blowing (MB).

Principle and structure. In the melt-blowing process, a thermoplastic polymer is melted in an extruder and forced through a linear die containing a row of fine orifices [8, p. 143S]. As shown in **Figure 2.2**, at the die exit, two convergent streams of hot air impinge symmetrically on the emerging polymer melt, exerting a drag force that rapidly attenuates it into microfibres. The fibres travel towards a rotating drum collector, solidifying as they encounter cooler ambient air, and accumulate as a self-bonded nonwoven mat [8, p. 143S]. The process is entirely solvent-free, which makes it inherently more sustainable than solution-based spinning methods. For effective fibre formation, the polymer must exhibit a sufficiently low melt viscosity; the typical melt flow index (MFI) range for melt-blowing is 15–3 000 $g/10\ min$ [8, p. 144S].

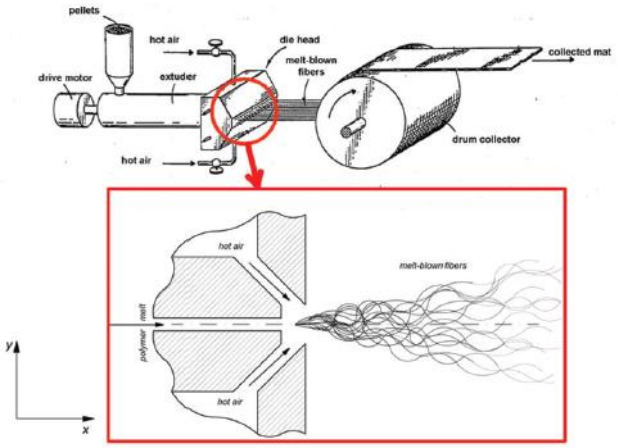

Figure 2.2. *Schematic of a typical melt-blowing line: polymer pellets are fed into an extruder, and the melt is forced through a die head where convergent hot-air jets attenuate it into microfibres collected on a rotating drum. The inset shows the die-tip detail with the symmetric air streams. Taken from [8, p. 143S, Fig. 1].*

Key parameters and effects. The morphology of melt-blown fibres is governed by several interrelated parameters. Increasing the air velocity (or the air-to-polymer mass ratio, C) reduces the mean fibre diameter but broadens the diameter distribution (higher coefficient of variation, CV) due to enhanced turbulence [8, pp. 148S–149S]. The die temperature has a pronounced effect: raising it from 250 to 300 °C has been reported to halve the average fibre diameter from approximately 12 to 6 µm [8, p. 152S]. The die-to-collector distance (DCD) controls the time available for attenuation; a larger DCD generally produces finer fibres but may reduce inter-fibre bonding and web strength because of lower contact temperatures [8, pp. 153S–154S]. These parameters collectively determine the pore structure of the resulting mat: higher air pressure yields smaller pores with denser packing, thereby increasing the pressure drop (ΔP) across the medium [8, pp. 150S–151S].

Hybrid variants: SBS → MB. Solution blow spinning (SBS) generates nanofibers by injecting a polymer solution through concentric nozzles surrounded by a high-velocity air stream, without requiring a high-voltage electric field [9, p. 19615]. Song et al. demonstrated a continuous roll-to-roll SBS line capable of producing 500 mm-wide nanofiber membranes, using a polyacrylonitrile (PAN) solution (12 wt% in DMSO) delivered at 130 mL/h with air at 40–60 kPa and 100–120 m/s [9, pp. 19617–19618]. By depositing SBS nanofibres directly onto a melt-blown electrostatic substrate, the authors obtained a hybrid SBS–MB filter whose filtration efficiency rose from 83.4% to 95.5%, while the pressure drop increased only moderately from 21.7 to 29.1 Pa [9, p. 19619]. The adhesion between layers is facilitated by residual solvent at the moment of impact, yielding a bond strength of approximately 80 N/m^2 [9, p. 19619]. Although SBS offers access to the sub-100 nm fibre regime, its reliance on organic solvents limits its sustainability compared with melt-blowing.

Additive manufacturing (AM) by extrusion.

FFF vs FGF. Additive manufacturing (AM) via material extrusion provides an alternative route for producing polymeric structures with complex three-dimensional geometries. Two main variants exist: fused filament fabrication (FFF), which feeds a solid filament through a heated nozzle (typical diameter 0.1–0.5 mm, throughput < 0.5 kg/h), and fused granulate fabrication (FGF), which employs a screw extruder fed with pellets, achieving deposition rates up to 80 kg/h—roughly 200 times those of FFF [10, pp. 10–11]. FGF reduces raw-material costs by more than an order of magnitude and enables the direct use of recycled thermoplastics without significant loss of mechanical properties [10, pp. 11, 31].

Print orientation. The build orientation significantly affects the mechanical performance of printed parts. Traditional layer-by-layer (vertical) deposition is limited by the build height of the printer and may require the division of large objects into sub-parts, introducing potential weak joints. Lateral (infinite-build) approaches, in which layers are oriented vertically via a conveyor system, allow a theoretically unlimited build length and reduce material sagging [10, pp. 18–19].

Speed/finish trade-offs. A fundamental trade-off exists between throughput and surface quality: larger nozzle diameters increase the volumetric deposition rate but worsen the surface finish due to the stair-stepping effect; solutions such as variable-diameter nozzles and multi-resolution robotic systems with two simultaneous manipulators have been proposed to address this compromise [10, pp. 21–23].

Comparative conclusion. Table 2.2 summarises the main characteristics of the processing techniques discussed above. Among these, melt-blowing stands out for its combination of high throughput, solvent-free operation, and ability to produce microfibrous nonwoven mats in a single step. It is for these reasons that melt-blowing was selected to produce the PP nonwoven samples characterised in this thesis. The following sections turn to the theoretical framework underlying the electrical and piezoelectric behaviour of polymeric materials, beginning with the conduction mechanisms that govern charge transport and trapping in polymer dielectrics.

Table 2.2. *Comparative overview of processing techniques for polymeric fibre structures. Data compiled from [8, p. 143S] for MB, [9, p. 19618] for SBS, [10, p. 11] for AM and [11, p. 1] for S/M/N laminates.*

Technique	Strengths	Limitations	Typical output	Sustainability
MB	High throughput; sub-µm fibres; solvent-free	Thermoplastics only; narrow T window; fibre CV sensitive to turbulence	Nonwoven mats (1–10 µm)	High (no solvents, melt-based)
SBS / hybrid SBS–MB	Nanofibers (< 100 nm); continuous roll-to-roll; combinable with MB	Solvent-based; limited polymer range; adhesion dependent on residual solvent	Nanofiber layers on MB substrates	Moderate (solvent use)
AM – FGF	Scalable (1–80 kg/h); recyclable pellets; complex geometries; > 10×cost reduction	Mechanical anisotropy; stair-stepping surface finish; slow for very large volumes	3D parts (mm-scale features)	High (recyclable feedstock)
S/M/N laminates	Tuneable porosity; layered functionality; high filtration efficiency	Rapid clogging; limited dust-holding capacity	Multi-layer filter media	Variable

2.2 Conduction mechanisms in polymeric materials

2.2.1 Electrode-limited conduction mechanisms

Introduction and background to ferroelectrets. The previous sections have established that isotactic polypropylene is the material of choice for the nonwoven structures investigated in this thesis and that melt-blowing is the processing route employed to produce them. To understand the piezoelectric behaviour of these structures, however, it is essential to examine how electric charges are injected into, transported through, and trapped within the polymer. In ferroelectrets—porous polymer films in which dielectric barrier discharges (DBD) deposit charges of opposite polarity on the internal surfaces of gas-filled cavities—the resulting macroscopic dipoles give rise to a measurable piezoelectric coefficient d_{33}[12, pp. 1–2].

The stability of this piezoelectric response is ultimately governed by the balance between charge injection at the electrode–polymer interface and charge transport and trapping in the bulk. Conduction mechanisms in dielectrics are accordingly classified into two families: electrode-limited mechanisms, which depend on the properties of the metal–dielectric interface and control how carriers are injected into the material, and bulk-limited mechanisms, which depend on the material's internal structure and govern carrier transport within the volume [13, p. 2]. This section addresses the first family; the second is treated in **Section 2.2.2**.

Schottky (thermionic) emission. At temperatures above 0 K, a fraction of the conduction electrons in the metal electrode possesses kinetic energy sufficient to overcome the potential-energy barrier at the metal–dielectric interface [13, p. 2]. When an external electric field is applied, the barrier height is reduced by the Schottky effect—an image-force lowering proportional to the square root of the field [13, p. 3]. The resulting current density is described by the Richardson–Schottky equation:

$$J = A^{*}T^{2}exp\left\{\frac{-q[\phi_B - \beta_S]}{kT}\right\} \quad (2.1)$$

where J is the current density, A^{*} is the effective Richardson constant (120 $m^{*}/m_0 A \cdot cm^{-2} \cdot K^{-2}$), T is the absolute temperature, q is the elementary charge, $q\phi_B$ is the Schottky barrier height, $\beta_S = \sqrt{q^3/4\pi\varepsilon_r\varepsilon_0}$ is the Schottky coefficient—where E is the applied electric field, ε_r is the relative dielectric constant and ε_0 is the vacuum permittivity—and k is the Boltzmann constant. [13, p. 3]. The mechanism is experimentally identified by verifying that a plot of $ln(J/T^2)$ vs $E^{1/2}$ yields a straight line, whose slope provides information on the barrier height and the dielectric constant [13, p. 3]. Schottky emission is the dominant electrode-

limited mechanism at moderate electric fields and elevated temperatures; it is therefore particularly relevant to the thermal stability of the trapped charge in ferroelectrets, where temperature-driven de-trapping governs the decay of the piezoelectric coefficient [12, p. 4].

Fowler–Nordheim (F–N) tunnelling. At very high electric fields, the potential barrier at the metal–dielectric interface is deformed into a narrow triangle through which electrons can quantum-mechanically tunnel without requiring thermal activation [13, p. 5]. This mechanism becomes significant when the barrier thickness is reduced to approximately 100 Å or less, corresponding to fields of the order of $10^{10}\ V/m$. The current density is given by:

$$J = \frac{q^3 E^2}{8\pi h q \phi_B} exp\left\{\frac{-8\pi(2qm_T^*)^{1/2}\phi_B^{3/2}}{3hE}\right\} \quad (2.2)$$

where h is Planck's constant and m_T^* is the effective tunneling mass in the dielectric [13, p. 5]. Unlike Schottky emission, F–N tunneling is essentially independent of temperature, making it dominant under high-field, low-temperature conditions. Experimentally, the mechanism is identified from the linearity of a $ln(J/E^2)$vs $1/E$ plot [13, p. 5]. The two mechanisms are thus complementary: Schottky emission prevails when thermal energy drives carriers over the barrier, whereas F–N tunneling prevails when the field narrows the barrier sufficiently for quantum-mechanical penetration.

Other electrode-limited mechanisms. Two additional mechanisms deserve mention for completeness, although their relevance to bulk polymer dielectrics is limited. Direct tunnelling occurs when the dielectric is thin enough (< 3.5 nm) for electrons to traverse its entire thickness through a trapezoidal barrier; this regime is significant in ultra-thin gate oxides but not in the relatively thick PP nonwovens considered here [13]. Thermionic-field emission represents an intermediate case in which electrons possess enough thermal energy to reach an elevated level within the barrier, from which they tunnel through a reduced thickness; it bridges the Schottky and F–N regimes and is observed at intermediate fields and temperatures [13].

Closing note on the coefficient β_S. The Schottky coefficient β_S introduced in **Equation 2.1** will be revisited in **Section 2.2.2**, where a mathematically analogous but physically distinct coefficient arises in the context of bulk-limited conduction.

2.2.2 Bulk-limited conduction mechanisms

Opening and framing. Once charge carriers have been injected across the electrode–dielectric interface by the mechanisms described in **Section 2.2.1**, their subsequent transport is governed by the internal structure of the polymer—by the density, depth, and spatial distribution of localised electronic states (traps) within the amorphous and crystalline regions. The resulting bulk-limited conduction mechanisms determine how far and how fast carriers move through the dielectric volume and, ultimately, control the long-term stability of the trapped charge that underpins the piezoelectric response of ferroelectrets [13, p. 2].

Poole–Frenkel (P–F) emission. The Poole–Frenkel effect is the bulk analogue of Schottky emission: an external electric field lowers the Coulombic barrier surrounding a trapped carrier, thereby increasing the probability of its thermal release into the conduction band [13, p. 8]. The barrier-lowering coefficient $\beta_{PF} = \sqrt{q^3/\pi\varepsilon_r\varepsilon_0}$ is mathematically identical to the Schottky coefficient β_S introduced in **Section 2.2.**1; despite this equivalence, the physical origin is fundamentally different, since Schottky emission concerns injection from the electrode, while Poole–Frenkel emission concerns the release of carriers already trapped within the bulk. The current density takes the form:

$$J = q\mu N_C E exp\left\{\frac{-q\left[\phi_T - \sqrt{qE/\pi\varepsilon_i\varepsilon_0}\right]}{kT}\right\} \quad (2.3)$$

where μ is the drift mobility, N_C is the effective density of states in the conduction band, $q\phi_T$ is the trap energy level, and ε_i is the dielectric constant of the insulator [13, p. 8]. The barrier-lowering coefficient β_{FF} is mathematically identical to β_S of Schottky emission but describes de-trapping *within* the bulk rather than injection from the electrode. Experimentally, the mechanism is identified from the linearity of a plot of ln(J/E) versus $E^{1/2}$ [13, p. 9].

Space-charge-limited conduction (SCLC). When the rate of charge injection exceeds the transport capacity of the bulk, the excess carriers accumulate near the injecting electrode and form a space-charge region that locally distorts the electric field and limits further current flow. The conduction behaviour progresses through three regimes as the applied voltage increases. At low voltages, the current is ohmic ($J \propto V$) because the injected charge is small relative to the thermally generated carriers [13, p. 13]. Above a transition voltage, the injected charge fills the available trap states, and the current follows a modified Child's law:

$$J = \frac{9}{8}\varepsilon\mu\theta\frac{V^2}{d^3} \quad (2.4)$$

where d is the specimen thickness, ε is the permittivity, and $\theta = n_{free}/n_{total}$ is the ratio of free to total (free + trapped) carriers [13, p. 13]. When the voltage reaches the trap-filled limit (V_{TFL}), all traps are saturated and the current jumps abruptly to the trap-free Child's law ($J = 9\varepsilon\mu V^2/8d^3$, with $\theta = 1$). In a $\log J$ vs $\log V$ plot, the three regimes appear as straight-line segments with slopes of 1, 2, and 2 (shifted upward), the sharp transition at V_{TFL} being a hallmark of SCLC [13, p. 13]. This mechanism is directly relevant to the formation of homo-charges (same polarity as the nearby electrode, producing a shielding effect) and hetero-charges (opposite polarity, intensifying the local field), both of which influence the long-term charge stability and, hence, the piezoelectric performance of ferroelectrets [13, p. 14].

Hopping conduction. In disordered regions of the polymer, carriers can advance by thermally activated tunnelling between adjacent localised states. The hopping current density is expressed as shown below:

$$J = qanvexp\left\{\frac{qaE - E_a}{kT}\right\} \quad (2.5)$$

where a is the mean hopping distance, n is the carrier concentration, ν is the thermal vibration frequency, and E_a is the activation energy from the trap to the conduction band. Because hopping depends on both the inter-site distance and the trap-depth distribution, it is strongly influenced by the degree of crystallinity and the morphology of the amorphous phase [13, p. 10].

Ohmic and ionic conduction. At low electric fields and in the absence of significant charge injection, transport follows Ohm's law ($J = qn\mu E$), where the conductivity σ depends only on the thermally generated carrier concentration [13, p. 10]. A parallel contribution arises from ionic conduction, driven by the drift of ions originating from residual impurities, additives, or absorbed moisture. Ionic transport occurs preferentially in the amorphous phase; its mobility increases markedly with temperature and decreases with increasing crystallinity [13, p. 15].

Implications for charge stability in ferroelectrets. The bulk-limited mechanisms described above collectively determine how rapidly the trapped charge—and therefore the piezoelectric coefficient d_{33}—decays at elevated temperatures. In melt-blown PP fibres corona-charged at −2 kV, the surface-potential decay follows a thermally activated release from traps whose energy spectrum can be reconstructed via the Simmons model; untreated PP exhibits shallow traps that begin to empty near room temperature, whereas treatment of the granules with

orthophosphoric acid (H_3PO_4) prior to extrusion generates deep traps centred at approximately 1.3 eV, shifting the onset of charge decay upward by 40 °C [14, pp. 33, 36]. A similar strategy has been applied to LDPE ferroelectrets, where the d_{33} of untreated samples decays already at 100 °C due to the intrinsically lower stability of positive charges; H_3PO_4 treatment shifts the charge-decay curves by 60 K and the d_{33} curves by 40 K towards higher temperatures [15, pp. 1, 3]. In FEP-based ferroelectrets with template-formed tubular channels, treatment with $TiCl_4$ vapour shifts the d_{33} decay by a further 60 °C, yielding negligible degradation up to 150 °C and a residual 30% of the initial value at 200 °C—far exceeding the thermal stability achievable with PP [16, pp. 1, 3]. These findings demonstrate that the thermal stability of the piezoelectric response is not an intrinsic material limit but can be engineered by modifying the trap-energy spectrum through chemical surface treatments [14, p. 36], [15, p. 3], [16, p. 3].

Conclusion. Together with the electrode-limited mechanisms of Section 2.2.1, the bulk-limited processes discussed here define the physical framework within which charges are injected, transported, trapped, and eventually lost in polymer dielectrics [13, p. 2]. This framework is a prerequisite for understanding the piezoelectric effect in polymers, which is the subject of the following sections.

2.3 Piezoelectric properties of polymeric materials

2.3.1 Fundamentals of piezoelectricity

Historical background and fundamental definitions. The conduction and trapping mechanisms discussed in **Sections 2.2.1** and **Section 2.2.2** govern how electric charges are deposited and retained in polymer dielectrics. The present section introduces the physical phenomenon that exploits those trapped charges to produce a useful electromechanical response: piezoelectricity. The piezoelectric effect was discovered in 1880 by Pierre and Jacques Curie, who observed that certain crystals—notably quartz (SiO_2)—develop surface charges when subjected to mechanical stress [17, p. 1]. The direct piezoelectric effect consists in the generation of an electric displacement (or charge) proportional to an applied mechanical stress, while the converse (inverse) effect consists in the development of a mechanical strain proportional to an applied electric field [17, pp. 2–3]. These two effects are the physical basis for sensing and actuation applications, respectively, and the conversion efficiency between mechanical and electrical energy is what makes piezoelectric materials attractive for energy harvesting.

Historically quartz was the first widely used piezoelectric material but the discovery of barium titanate ($BaTiO_3$) during the Second World War marked a turning point: when poled under a high voltage, $BaTiO_3$ exhibited a piezoelectric response approximately 100 times larger than that of quartz [17, p. 1]. In 1954, the lead zirconate titanate system (PZT, $PbTiO_3 - PbZrO_3$) was found to possess piezoelectric constants roughly twice those of $BaTiO_3$ and a Curie temperature exceeding 300 °C, making it the dominant commercial piezoelectric material to date, particularly near the morphotropic phase boundary (MPB) at a Zr/Ti ratio of 52/48 [17, p. 1]. However, PZT contains more than 60 wt% lead, which has prompted intensive research into lead-free alternatives, including piezoelectric polymers [17, p. 2].

Constitutive relations and piezoelectric coefficients. Piezoelectricity is described as a linear electromechanical interaction in which the coupling between the mechanical and electrical domains is expressed by the piezoelectric coefficient d, a third-rank tensor that relates a vector (electric displacement D or electric field E) to a second-rank tensor (stress T or strain S) [17, p. 3] [18, p. 10]. In the most used form (the d-form), the coupled constitutive equations are:

$$D_i = d_{ijkl}T_{kl} + \varepsilon_{ik}^{T}E_k \ (2.6\ a)$$

$$S_{ij} = s_{ijkl}^{E}T_{kl} + d_{kij}E_k \ (2.6\ b)$$

where D_i is the electric displacement (C/m^2), T_{kl} is the stress (N/m^2), E_k is the electric field (V/m), S_{ij} is the strain (dimensionless), d_{kij} is the piezoelectric charge constant $(pC/N\ or\ pm/V)$, ε_{ik}^{T} is the dielectric permittivity at constant stress, and s_{ijkl}^{E} is the elastic compliance at constant electric field [17, p. 4] [18, p. 10]. In the Voigt notation, the paired tensor indices *ij* are replaced by a single index *m* = 1–6 (where 1–3 correspond to normal stresses along x_1, x_2, x_3 and 4–6 to shear stresses T_{23}, T_{13}, T_{31}), reducing the notation to a practical matrix form [17, p. 4] [18, p. 8].

Four sets of piezoelectric coefficients are defined, depending on which pair of variables is chosen as independent [17, p. 4] [18, p. 10]:

- The charge constant d_{ij} (pC/N) quantifies the charge developed per unit applied stress (direct effect) or, equivalently, the strain per unit applied field (converse effect) [17, p. 8].
- The voltage constant g_{ij} (Vm/N) quantifies the electric field developed per unit stress under open-circuit conditions; it is related to d by $g = d/\varepsilon$ [17, p. 8].
- The stress piezoelectric constant e_{ij} and the stiffness constant h_{ij} complete the set, corresponding to the e- and h-forms of the constitutive equations [18, p. 10].

For the purposes of this thesis, the most relevant coefficient is d_{33}, which applies when both the applied force and the collected charge are directed along the polarisation axis (direction 3). A secondary coefficient, d_{31}, describes the charge collected along axis 3 when the force is applied perpendicularly with respect to that axis; the empirical relation $d_{33} \approx -2.5 \cdot d_{31}$ is commonly used for ceramics [17, p. 8].

The electromechanical coupling factor k provides a global measure of the efficiency of energy conversion between the mechanical and electrical domains: k^2 equals the ratio of converted energy to applied energy [17, p. 8] [18, p. 44]. A related quantity is the mechanical quality factor $Q_m = f_r/(f_2 - f_1)$, which characterises the sharpness of the resonance peak and is inversely related to mechanical losses [17, p. 9] [18, p. 50].

Crystal symmetry, ferroelectricity and poling. The existence of piezoelectricity in a material is dictated by its crystal symmetry. Of the 32 crystallographic point groups, 21 lack a centre of symmetry; of these, 20 are piezoelectric (the cubic class 432 being the sole non-centrosymmetric exception) [17, p. 4]. A subset of 10 classes possesses a spontaneous polar axis and therefore exhibits pyroelectricity—a change in polarisation with temperature. Within the pyroelectric group, materials whose spontaneous polarisation can be reversed by an external electric field are classified as ferroelectric [17, p. 4]. This hierarchy—dielectrics ⊃ piezoelectrics ⊃ pyroelectrics ⊃ ferroelectrics—is illustrated in **Figure 2.3**.

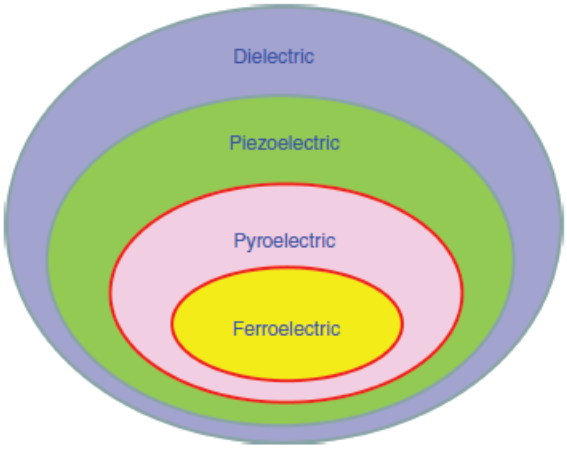

***Figure 2.3**. Hierarchical classification of dielectric materials. All ferroelectrics are pyroelectric, all pyroelectrics are piezoelectric, but the converse is not true. The non-centrosymmetric crystal symmetry is the necessary condition for piezoelectricity. Taken from [17, p. 4, Fig. 1.2].*

polarisation P_r (the polarisation remaining after the field is removed), and the coercive field E_c (the field required to reduce the polarisation to zero) [17, p. 5]. In polycrystalline ceramics such as PZT, a poling process (application of a strong DC field ($E > E_c$) at elevated temperature) is required to align the domains along the field direction; upon removal of the field, most domains

retain their orientation, conferring a macroscopic piezoelectric response to the material. This poled state is thermally stable up to the Curie temperature T_c, above which the material loses its ferroelectric character [17, pp. 6–7].

The symmetry requirement of non-centrosymmetry also dictates which components of the d tensor are non-zero: for example, poled ceramics and poled PVDF films are described by the crystal class 6 mm, which yields three independent piezoelectric constants ($d_{33}, d_{31} = d_{32}, d_{15} = d_{24}$) [18, pp. 1, 21, 24]. In semicrystalline polymers such as PVDF, the polarisation arises from dipolar alignment of the crystalline β-phase; in ferroelectrets, by contrast, the macroscopic dipoles originate from charges trapped on cavity surfaces, as discussed in **Section 2.2.1**. The specific mechanisms by which polymers acquire piezoelectric properties are treated in **Section 2.3.2**.

Measurement of piezoelectric parameters. The quasi-static (Berlincourt) method is the most widespread technique for determining d_{33}: a low-frequency sinusoidal force is applied to the sample, and the generated charge is measured and divided by the applied force to yield d_{33} directly. The measurement is rapid and requires simple instrumentation, making it the standard method for routine quality assessment [17, p. 10] [18, p. 47]. The inverse piezoelectric (laser interferometry) method applies a known electric field and measures the resulting strain with a laser interferometer; being a non-contact technique, it is particularly suited to thin films and avoids mechanical clamping artefacts [17, p. 12]. For a complete characterisation of all piezoelectric, elastic, and dielectric constants, resonance–anti-resonance measurements are employed on specimens of standardised geometry (bars, discs, plates). The frequencies of the impedance minimum (f_r, resonance) and maximum (f_a, anti-resonance) are related to the coupling factor k and, through the known geometry, to the full set of material constants according to IEEE Standard 176 [18, pp. 46, 51].

Summary and bridge toward polymer systems. In summary, the linear constitutive equations, the symmetry requirements, and the standardised measurement protocols reviewed in this section provide the common theoretical and metrological framework for comparing piezoelectric materials—whether inorganic ceramics, single crystals, or polymers. The following section discusses how polymeric materials, and in particular polypropylene, can be made to exhibit piezoelectric behaviour, bridging the fundamental concepts introduced here with the experimental investigations presented in subsequent chapters.

2.3.2 Polymers as piezoelectric materials

Performance Benchmarking: Ceramic vs. Polymers. The previous section established the theoretical framework of piezoelectricity—constitutive equations, symmetry requirements, and measurement protocols—using inorganic ceramics as the primary reference. Ceramic materials such as PZT ($d_{33} \approx 593\,pC/N$) and $BaTiO_3$ ($d_{33} \approx 190\,pC/N$) offer outstanding piezoelectric coefficients [19, p. 5] [24, p. 30]. However, they are intrinsically brittle, dense, and—in the case of PZT—contain more than 60 wt% lead, posing serious environmental and biocompatibility concerns [19, p. 5] [21, p. 5]. These limitations have motivated a sustained effort to develop polymeric alternatives that combine adequate piezoelectric response with mechanical flexibility, low density, and ease of processing [21, p. 1].

Landmark Discovery: PVDF and the Kawai (1969) Report. A turning point was Kawai's 1969 report of piezoelectricity in mechanically stretched and electrically poled poly(vinylidene fluoride) (PVDF) thin films, establishing polymer films as viable electromechanical materials [20, p. 975]. In particular, after repeated mechanical stretching at 100–150 °C, followed by the application of a static electric field of approximately 300 kV/cm (while the temperature was gradually increased from room temperature to 90 °C), PVDF exhibited a piezoelectric effect recorded in the coefficient $d_{31} = 10 - 20 \cdot 10^{-8}$ (c.g.s.) [20, pp. 975–976]. Making the appropriate conversion from the c.g.s. system to the SI system, this corresponds to $d_{31} = 3.3 - 6.7\,pC/N$ and, according to the empirical relation $d_{33} \approx -2.5 \cdot d_{31}$ introduced in **Section 2.3.1**, an estimated d_{33} in the range of $8 - 17\,pC/N$ [20, pp. 976]. Kawai also observed weak piezoelectric effects in polycarbonate, polyethylene, and polytetrafluoroethylene, but found no measurable response in polystyrene, polyester, or nylon-6 [20, p. 976]. This discovery opened an entirely new class of electromechanical materials—piezoelectric polymers—which can be broadly divided into three families: intrinsic piezoelectric polymers (led by PVDF), piezoelectric polymer–ceramic composites, and ferroelectrets (piezoelectrets) [19, p. 3].

Intrinsic Piezoelectric Polymers: Phases and Copolymers. PVDF is a semicrystalline fluoropolymer that can exist in at least four crystalline phases, commonly designated α, β, γ, and δ [21, p. 10]. The α-phase is the most thermodynamically stable and forms readily upon cooling from the melt, but it is non-polar because its chain conformation (TGTG') results in the cancellation of the dipole moments of the C–F bonds. The β-phase adopts an all-trans (TTTT) planar-zig-zag conformation in which all C–F dipoles are aligned in the same direction, yielding the highest net dipole moment per unit cell and, consequently, the strongest piezoelectric response [21, p. 10]. Conversion from the α- to the β-phase is typically achieved by mechanical

stretching (uniaxial or biaxial drawing at temperatures below the melting point), followed by electrical poling under a strong DC field to orient the dipolar domains along the field direction [19, p. 20]. The copolymer P(VDF–TrFE) is of particular interest because it crystallises directly into the ferroelectric β-phase without the need for mechanical stretching, simplifying the manufacturing process [19, p. 20].

The γ-phase, with an intermediate conformation (TsTsG'), exhibits moderate polarity and can form at high crystallisation temperatures or under specific solvent conditions; the δ-phase is the polar analogue of the α-phase, obtainable by poling α-phase films at very high fields [21, p. 10]. While the γ- and δ-phases contribute some piezoelectric activity, the β-phase remains the primary target of processing because it possesses the largest spontaneous polarisation per unit cell [21, p. 10].

Modern PVDF films achieve a piezoelectric coefficient [19, p. 5] and a coupling factor [24, p. 30]. These values are one to two orders of magnitude lower than those of PZT, but the polymer offers decisive advantages in terms of mechanical flexibility, low density, chemical resistance, and processability into thin films, fibres, and coatings [19, p. 5] [24, p. 5]. For applications in which a high voltage sensitivity rather than a high charge output is required, the low ε_r of PVDF is beneficial, since the voltage constant $g = d/\varepsilon$ is inversely proportional to the permittivity [19, p. 11]. PVDF therefore remains the benchmark polymer for flexible piezoelectric sensors and wearable energy harvesters.

Hybrid Architectures: Polymer–Ceramic Composites. An intermediate approach consists in dispersing a ceramic filler (PZT, $BaTiO_3$, ZnO, or KNN) within a polymer matrix to combine the high piezoelectric coefficients of the inorganic phase with the flexibility of the organic phase [21, p. 1]. The resulting composites are classified by their connectivity—the geometric arrangement of the two phases. In 0–3 composites, discrete ceramic particles are randomly dispersed in a continuous polymer matrix; in 1–3 composites, aligned ceramic fibres or pillars are embedded in the polymer; in 2–2 composites, alternating planar layers of ceramic and polymer are stacked [21, pp. 6–8]. PVDF is the preferred matrix material because its relatively high dielectric constant (6–13) maximises charge accumulation at the filler–matrix interface [21, p. 10]. Composite values typically fall between 10–100 pC/N, providing an intermediate performance bracket between pure polymers and ceramics [21, p. 11].

Ferroelectrets (Piezoelectrets): Mechanism and Cellular Structures. A fundamentally different route to polymer piezoelectricity is offered by ferroelectrets (also called

piezoelectrets), which are cellular or voided polymer structures in which the piezoelectric response arises not from molecular dipoles but from electric charges trapped on the internal surfaces of gas-filled cavities [22, p. 1]. The charging mechanism relies on dielectric barrier discharge (DBD): when a sufficiently strong electric field is applied across the structure, the gas inside the cavities undergoes Paschen breakdown, ionising its molecules and driving charges of opposite polarity onto the upper and lower walls of each cavity [22, p. 2]. Each charged cavity thus acts as a macroscopic dipole. When the structure is subjected to a mechanical stress, the cavities deform, changing the distance between the trapped charges and producing a measurable change in surface charge—i.e. a direct piezoelectric effect (**Figure 2.4**) [22, p. 2]. Unlike PVDF, where the effect is intrinsic (molecular dipoles), in ferroelectrets the effect is extrinsic (space charges); nevertheless, the macroscopic description in terms of d_{33} remains valid [22, p. 1].

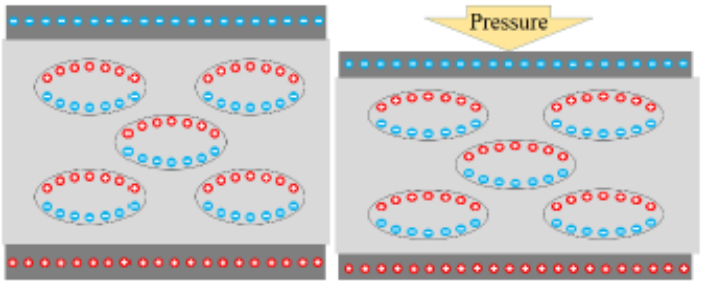

***Figure 2.4**. Piezoelectric mechanism in ferroelectrets. Left: charges of opposite polarity stably trapped on the internal walls of a gas-filled cavity after dielectric barrier discharge (DBD). Right: under applied pressure the cavity deforms, reducing the charge separation and generating a measurable electrical signal. Taken from [22, p. 2, Fig. 6].*

The most widely studied ferroelectret material is cellular polypropylene (PP), commercially available as EMFi® film: biaxially stretched and inflated PP foams have reached values exceeding 600 pC/N—significantly higher than PVDF and comparable to soft PZT ceramics [22, p. 2]. However, the thermal stability of PP ferroelectrets is limited: the trapped charge, and consequently the piezoelectric coefficient, begins to decay at temperatures as low as 60 °C due to the relatively shallow trap states in polypropylene [22, p. 2] [23, p. 1668]. Fluoropolymer-based ferroelectrets offer substantially improved thermal stability: FEP–PTFE–FEP laminated structures have achieved values of approximately 1,000 pC/N with negligible degradation up to 120–150 °C [22, p. 4]. Other materials investigated include polyethylene naphthalate (PEN, stable to approximately 80 °C) and low-density polyethylene (LDPE) [22, p. 2].

Advanced Fabrication and Nonwovens.

Fabrication of PP ferroelectrets by 3D printing. A recent development is the fabrication of PP ferroelectrets by fused filament fabrication (FFF), which offers precise control over cavity geometry in a single manufacturing step [23, p. 1668]. Assagra et al. produced a trilayer structure consisting of two solid PP layers (100 µm each) enclosing a central layer with an 80% infill triangular pattern that defines the cavity geometry; although designed for 300 µm, the final thickness was approximately 150 µm due to shrinking during cooling [23, pp. 1669-1670]. After printing, the structure was corona-charged at 3.0 kV DC for 10 s to induce DBD [23, p. 1670]. The initial reached 200 pC/N and decayed by roughly 40% over the first 20 days, stabilizing at 130 pC/N [23, p. 1671]. The thermal behavior mirrors conventional PP: the response is stable up to 60 °C, decreases by 17% at 80 °C, and drops below 40% after one hour at 100 °C [23, p. 1671]. At applied pressures above 20 kPa, the effect decreases because the cavities stiffen under static compression [23, p. 1671].

Laminates, multilayer structures, and nonwovens. Beyond cellular foams and 3D-printed structures, several laminate architectures have been explored to tune the piezoelectric and filtration properties of polymer ferroelectrets. FEP–PTFE–FEP stacks produced by template-based lamination have demonstrated the highest values reported for polymer ferroelectrets (1000 pC/N) [22, p. 4], while spunbond–melt-blown–spunbond (S/M/S) laminates allow independent control of porosity, air permeability, and mechanical strength through the selection of individual layer weights and fibre diameters [22, p. 2]. The key advantage of laminate architectures is their tunability: by varying the number of layers, the cavity size, and the polymer type, the piezoelectric response, the mechanical stiffness, and the thermal stability can be independently optimised for a given application [22, p. 4]. The melt-blown layer, with its fine-fibre, highly porous microstructure (typical fibre diameters of 2–10 µm), is of particular interest for ferroelectret applications because it provides an intrinsic network of gas-filled voids that may serve as the cavity structure required for charge trapping and piezoelectric activity. This is precisely the configuration investigated in the present thesis: melt-blown PP nonwovens are corona-charged, and their piezoelectric behaviour is characterised as a function of temperature, providing a direct link between the bulk-limited charge-stability mechanisms and the macroscopic response.

Applications and Summary. The applications of ferroelectrets span a wide range of domains. Their high values and low acoustic impedance make them well suited for pressure and force

sensors, including cardiorespiratory monitoring patches, and for electro-acoustic transducers such as microphones and loudspeakers [22, p. 1]. More recently, ferroelectrets have attracted interest for energy harvesting from low-frequency mechanical vibrations, where their large charge output per unit force provides an advantage over PVDF-based devices at the expense of thermal operating range [22, p. 1; 24, p. 4]. For all these applications, the trade-off between piezoelectric sensitivity and thermal stability remains the central engineering challenge.

Table 2.3 summarises the key characteristics of the piezoelectric polymer families discussed above, with PZT included as a ceramic reference.

A note of caution is warranted when comparing the thermal limits listed in this table. For PVDF, the reported value of approximately 100 °C corresponds to the Curie temperature (T_C), i.e. the irreversible ferroelectric phase transition. However, β-PVDF has been reported to degrade when exposed to temperatures above 70 °C for extended periods of time [25, p. 5111]; under isotropic convective annealing lasting ten minutes or more, d_{33} losses of nearly 30 % at 100 °C have been documented [25, p. 5114]. This degradation has been attributed to the thermally activated release of trapped surface charge due to the destabilisation of semi-crystalline polymer domains, rather than to a crystalline β→α phase transition [25, pp. 5111, 5117]. For PP ferroelectrets, the ≈60 °C limit refers instead to the onset of charge de-trapping from cavity surfaces. Although the microscopic origin of the charges differs—compensation charges bound to molecular dipoles in PVDF versus corona-injected charges trapped on cavity walls in PP—the macroscopic phenomenology is comparable: in both cases, thermally activated charge release governs the practical onset of piezoelectric decay. Therefore, the two thermal limits reported in the table reflect different physical quantities and should not be compared at face value.

Table 2.3. *Comparative overview of piezoelectric polymer families and PZT ceramic as reference. The d_{33} values and thermal limits are indicative ranges compiled from the sources cited from [19, p. 5], [21, p. 11], [22, pp. 2–4], [23, p. 1668] and [24, p. 30].*

Family	Piezoelectric mechanism	d_{33} (pC/N)	Thermal limit	Flexibility
PVDF / P(VDF–TrFE)	Molecular dipoles (β-phase)	20–33	$T_c \approx 100$ °C[a]	High
Polymer–ceramic composites (0–3)	Ceramic filler in polymer matrix	10–100	Depends on filler	Moderate
Ferroelectrets—PP (cellular / 3D-printed)	Trapped charges (DBD in cavities)	200–600	≈60 °C	High
Ferroelectrets—FEP / PTFE laminates	Trapped charges (DBD in channels)	270–1 000	120–150 °C	Moderate

Family	Piezoelectric mechanism	d_{33} (pC/N)	Thermal limit	Flexibility
PZT ceramic (reference)	Intrinsic (perovskite lattice)	≈593	$T_c > 300$ °C	None (brittle)

[a] Curie temperature (irreversible ferroelectric phase transition). Under prolonged isothermal exposure (≥ 10 min), the onset of measurable piezoelectric decay has been reported at approximately 70 °C [25, p. 5111].

The families of piezoelectric polymers reviewed in this section represent complementary trade-offs between performance, flexibility, and stability. PVDF provides the best overall compromise for thin-film flexible devices, combining moderate with excellent processability. Polymer–ceramic composites bridge the performance gap but at the cost of added density. Ferroelectrets offer the highest polymer-based values, but their thermal stability remains the principal limitation. The state-of-the-art review presented in this chapter—from the polymeric material and its processing, through the charge injection and trapping mechanisms, to the fundamentals of piezoelectricity—provides the scientific foundation for the experimental work described in the following chapters, in which melt-blown PP nonwovens are produced, corona-charged, and characterised to assess their piezoelectric response and its thermal stability.

3. METHODOLOGY AND RESEARCH ACTIVITIES

The theoretical framework established in **Chapter 2**—covering the functional properties of polypropylene, the conduction and charge-trapping mechanisms in polymer dielectrics, and the fundamentals of piezoelectricity—provides the basis for the experimental programme described in this chapter. Two Designs of Experiments (DoEs) were devised: the first is a process–factor screening aimed at identifying the sample configuration that maximises the piezoelectric coefficient d_{33} at room temperature (**Section 3.1.2**); the second investigates the thermal stability of the piezoelectric response through thermally stimulated charge-decay and temperature-dependent d_{33} measurements (**Section 3.1.3**). The chapter also describes the instrumentation employed (**Section 3.1.1**), the ancillary characterisation techniques—optical microscopy (**Section 3.1.4**) and surface hardness testing (**Section 3.1.5**)—and the processing steps applied to the PP fibre sheets prior to testing (**Section 3.2**).

3.1 Experimental techniques and instrumentations

3.1.1 Instrumentations used for the Designs of Experiments

The experimental programme relies on a set of instruments that can be grouped into four functional categories: **(i)** high-voltage DC power supplies for corona charging; **(ii)** an excitation and acquisition chain for the quasi-static measurement of the piezoelectric coefficient d_{33}; **(iii)** a non-contact electrostatic voltmeter for verifying the surface potential of the charged samples; **(iv)** a temperature-control system for the thermal characterisation. **Table 3.1** summarises the key specifications of each instrument; a more detailed description follows.

Table 3.1. *Summary of the instruments used in DoE 1 and DoE 2. Instruments marked with † are used only in DoE 2.*

#	Instrument	Model	Function	Key specification
1	DC power supply	FuG HCB 7–6500	Grid voltage (corona)	0 to ±6500 V, ±1 mA
2	DC power supply	FuG HCP 35–35000	Tip voltage (corona)	0 to 35 kV, 1 mA, 35 W
3	Waveform generator	Voltcraft FG-30802T	Excitation signal	1 µHz–80 MHz, 2 channels, DDS
4	Power amplifier	B&K Type 2718	Drive mini shaker	75 VA, 10 Hz–20 kHz
5	Conditioning amplifier	B&K Type 2692-C	Signal conditioning	100 nC input, 0.01–10 V/pC
6	Mini shaker	B&K Type 4810	Mechanical excitation	10 N, DC–18 kHz, 4 mm p-p
7	Force transducer	B&K Type 8230	Force + charge sensing (DoE 1)	110 mV/N, ±45 N, 75 kHz
8	Oscilloscope	Tektronix MDO34	Signal display + acquisition	4 channels, 5 GS/s, 10 Mpoints
9	Electrostatic voltmeter	Trek 341A	Surface potential measurement	±20 kV, ±0.1% FS

#	Instrument	Model	Function	Key specification
10	Temperature regulator †	G. MAIER R12/SSR/PT100	Thermal ramp control	Pt100 sensor, 3300 W, 230 V
11	Force transducer †	Burster 8435-5200	Force sensing (DoE 2)	±200 N, 1 mV/V, 5 kHz

High-voltage DC power supplies. Two FuG Elektronik units provide the high voltage required for corona charging. The FuG HCB 7–6500 is a bipolar supply (0 to ±6500 V, ±1 mA) with four-quadrant operation and power-sinking capability, used to set the grid potential that limits the charge deposited on the sample [26, pp. 41–42]. The FuG HCP 35–35000 is a unipolar supply (0 to 35 kV, 1 mA, 35 W) used to energise the corona needle; it features built-in voltage and current regulation with automatic mode transition, as well as short-circuit and flashover protection with adjustable overvoltage trip [26, pp. 19–20]. Both units are based on a switch-mode topology in which a fixed-frequency square-wave generator drives a transformer, followed by rectification and PWM-regulated filtering to produce the DC output.

Excitation and acquisition chain. The quasi-static d_{33} measurement employs a chain of five instruments. The Voltcraft FG-30802T waveform generator provides a programmable electrical excitation signal via direct digital synthesis (DDS), with a frequency range from 1 µHz to 80 MHz across two independent output channels [27]. Its output is fed to a Brüel & Kjær Type 2718 power amplifier (75 VA into a 3 Ω load, 10 Hz–20 kHz ±0.5 dB at 20 dB gain), whose current limit is continuously adjustable up to 1.8 A for the mini-shaker load [28, pp. 1–2]. The amplified signal drives a Brüel & Kjær Type 4810 mini-shaker, a compact permanent-magnet electrodynamic exciter with a radial-flexure suspension designed to produce near-rectilinear motion. The shaker is rated for a sine-peak force of 10 N in the 65 Hz–4 kHz range (7 N up to 18 kHz), with a maximum displacement of 4 mm peak-to-peak and a first armature resonance above 18 kHz [30, pp. 1–2].

In DoE 1, the force transducer used is the Brüel & Kjær Type 8230, a DeltaTron piezoelectric quartz sensor with integral electronics that converts the applied force into a low-impedance voltage output. Its key specifications are a voltage sensitivity of 110 mV/N, a full-scale range of ±45 N, and an unloaded mounted resonance frequency of 75 kHz [31, pp. 1–2]. In DoE 2, this transducer is replaced by the Burster 8435-5200, a strain-gauge full-bridge (Wheatstone) sensor with a calibrated range of ±200 N, a nominal bridge output of 1 mV/V, and a natural frequency of 5 kHz [37, pp. 1–2]; this sensor is preferred for DoE 2 because it allows both dynamic and static forces to be measured.

The signals from the force transducer are routed to a Brüel & Kjær Type 2692-C conditioning amplifier, a four-channel charge signal conditioner that converts the input charge into a

conditioned voltage output. It accepts a maximum differential charge input of 100 nC peak, with a selectable gain range from 0.01 to 10 V/pC, and supports high-pass cut-off frequencies of 0.1, 1, and 10 Hz and low-pass cut-off frequencies of 0.1, 1, 3, 10, 22.4, 30, and 100 kHz [29, pp. 1–3]. The conditioned signals are displayed and measured on a Tektronix MDO34 mixed-domain oscilloscope (4 analog channels, up to 5 GS/s sampling rate, 10 Mpoints record length) [32, pp. 1, 13].

Electrostatic voltmeter. The Trek 341A is a non-contact instrument for measuring surface electric potential based on a field-nulling technique, which provides DC-stable, high-accuracy measurements with reduced sensitivity to probe-to-surface spacing variations. Since model-specific documentation for the 341A is not publicly available, the closely related Model 341B is used here as a family-level reference: the measurement range is 0 to ±20 kV (DC or peak AC), with an accuracy better than ±0.1% of full scale and a speed of response of ≤200 µs for a 1 kV step [33, pp. 1–2].

Temperature-control system (DoE 2 only). The thermal characterisation employs a G. MAIER R12/SSR/PT100/3300/230 temperature regulator, which reads a Pt100 RTD sensor (compliant with DIN/IEC 60751, nominal resistance 100 Ω at 0 °C, temperature coefficient 0.00385 Ω/Ω/℃ between 0 and 100 °C) and modulates the power delivered to a heated metal plate through a time-proportional (duty-cycle) output driving a solid-state relay [34, pp. 4–5] [35]. The system is rated for 230 V AC, 15 A (3300 W) and is enclosed with protection class IP50 [36].

3.1.2 DoE 1 – Process–factor screening on PP nonwovens

Objective of the DoE. The objective of the first Design of Experiments is to measure the piezoelectric coefficient d_{33} of polypropylene fibre samples as a function of three factors: **(i)** P – phosphorus treatment (P−: untreated; P+: 30 wt% blend of H_3PO_4-treated pellets, 100 °C, 24 h); **(ii)** N – number of intermediate uncharged layers (N0: 0 layers; N1: 1 layer; N2: 2 layers; N3: 3 layers); **(iii)** V – charging voltage applied to the upper and lower layers (V1: ±2 kV; V2: ±4 kV; V3: ±5 kV). The factors P and N were selected because they most influence the softness—and hence the mechanical compliance—of the sample stacks, which is a determining parameter for the quasi-static measurement of d_{33}. In this screening stage, the d_{33} value recorded immediately after charging is considered, without accounting for the time-dependent decay at room temperature; this aspect is addressed in DoE 2.

Design of the DoE. For each of the 24 possible configurations (2 levels of P × 4 levels of N × 3 levels of V), the d_{33} measurement was repeated on three independent samples, yielding a total of 2 × 4 × 3 × 3 = 72 individual tests.

Responses of the DoE. For every configuration, two summary responses were extracted: **(i)** $d_{33,avg}$, the arithmetic mean of the three repetitions; **(ii)** $d_{33,avg,max}$, the highest $d_{33,avg}$ recorded among all configurations for each material type (P− and P+). To quantify the relative importance of each factor and their interactions on d_{33}, a full factorial analysis of variance (ANOVA) was performed on the 72 individual measurements, following the methodology described in [38, sec. 5.3.3.3, 5.5.9.3, 5.5.9.7]. The results are visualised through a main effect plot and a Pareto chart of standardised effects (F–values). A significance level of $\alpha = 0.05$ was adopted throughout.

.

Instrumentation and experimental setup. The work area is divided into three functional sections, as illustrated in the block diagram of **Figure 3.1**.

The electric charge section (**Figure 3.1a**) applies a corona discharge to the sample. A metal needle, energised at ±12 kV by the FuG HCP 35–35000 supply, generates the corona discharge. A metal grid, powered by the FuG HCB 7–6500 supply at one of the three voltage levels (±2, ±4, or ±5 kV), is interposed between the needle and the sample to limit the surface potential of the latter to the grid voltage. The maximum grid voltage is set to ±5 kV to prevent electrical breakdown of the sample, given the small needle-to-sample distance.

The d_{33} measurement section (**Figure 3.1b**) applies a sinusoidal mechanical force to the previously charged sample and records the resulting charge output. The Voltcraft FG-30802T waveform generator produces a 2 V peak-to-peak sine wave at 2 Hz, which is amplified by the B&K Type 2718 power amplifier (gain adjusted manually to obtain the desired force amplitude) and drives the B&K Type 4810 mini-shaker. The sample stack is placed on the B&K Type 8230 force transducer, which senses both the applied force and the charge generated by the sample. Both signals are routed to the B&K Type 2692-C conditioning amplifier, configured with the following conversion: 1 N → 1 V (force channel) and 1 pC → 10 mV (charge channel). The conditioned signals are displayed on the Tektronix MDO34 oscilloscope, and the piezoelectric coefficient is computed as the ratio of the peak-to-peak charge to the peak-to-peak force: $d_{33} = Q_{pp}/F_{pp}$.

The electrical potential measurement section (**Figure 3.1c**) uses the Trek 341A electrostatic voltmeter to verify, in a non-contact manner, that the corona-charged layers have reached the intended surface potential.

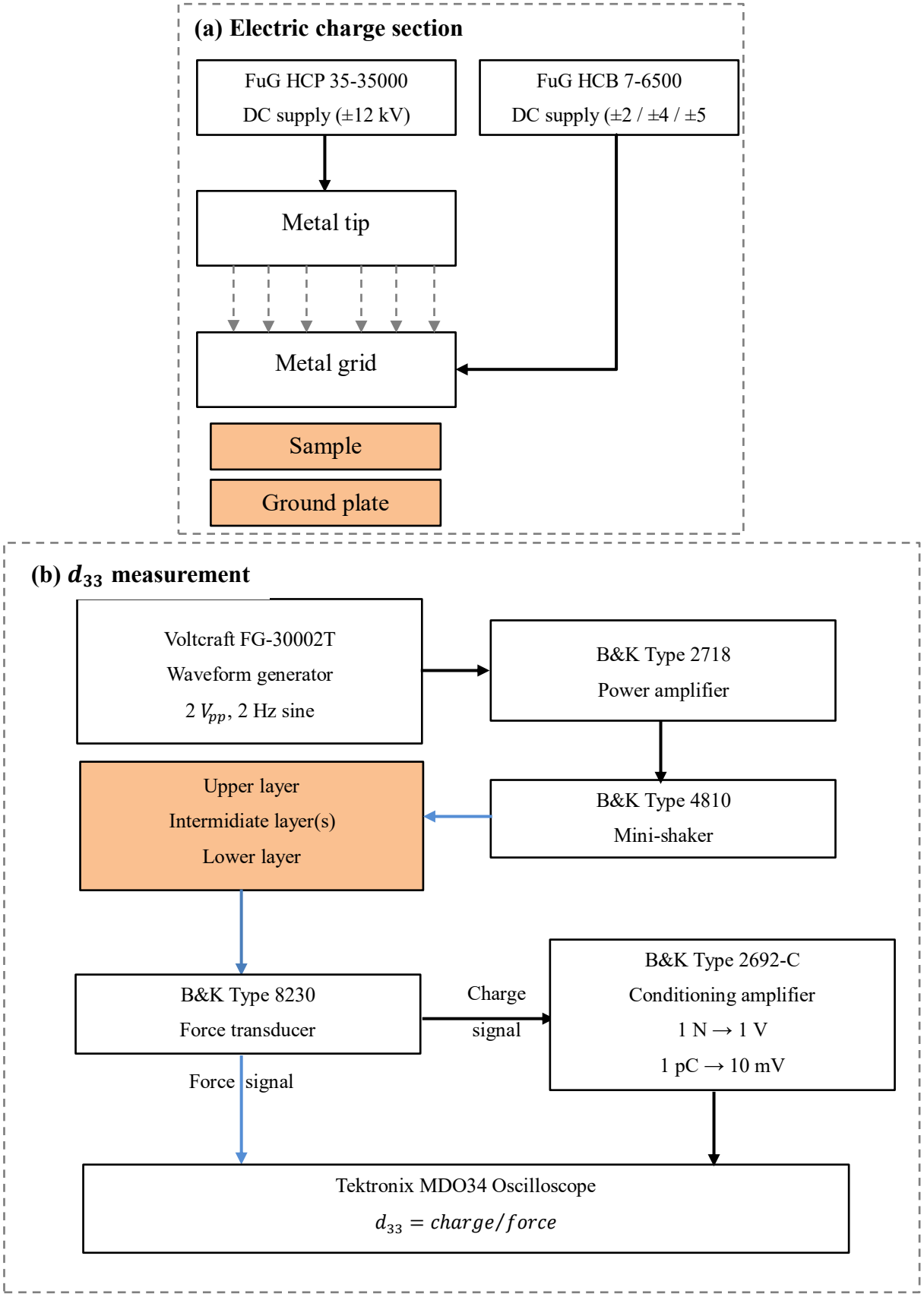

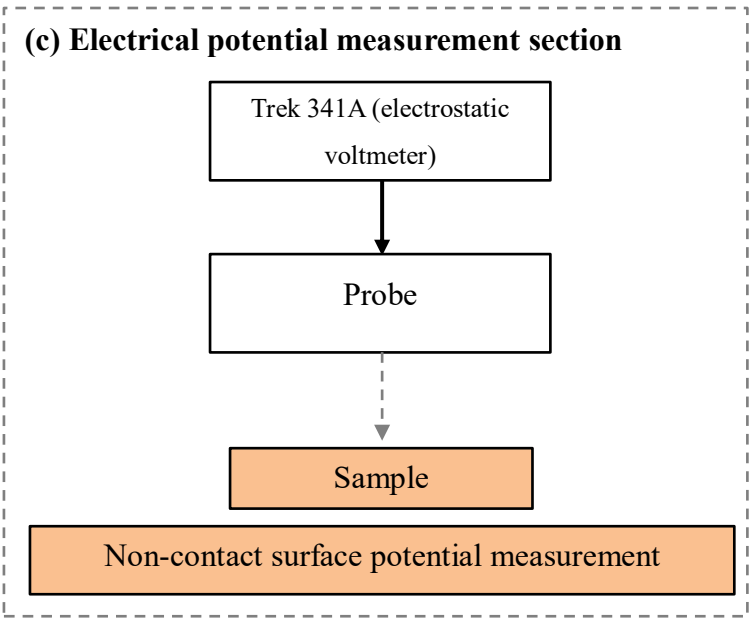

Figure 3.1 *Block diagram of the experimental setup used for DoE 1, comprising three functional sections: (a) electric charge section, (b) d_{33} measurement section, and (c) electrical potential measurement section. The signal flow is indicated by black arrows (electrical signal transferred through cables), blue arrows (mechanical signal) and dotted grey arrows (electrical signal transferred through air).*

Materials under test. The samples investigated in DoE 1 are melt-blown nonwoven discs (radius 25 mm) produced from a 50/50 wt% blend of two isotactic polypropylene grades, designated PP-A and PP-B. In the nomenclature adopted for this work, PP-A denotes a polypropylene random copolymer (PP-R): a grade in which ethylene co-monomer units are inserted randomly along the polypropylene backbone, resulting in a reduction of crystallinity and an increase in optical clarity and flexibility compared with the homopolymer. PP-B denotes a polypropylene block copolymer (PP-B): a grade in which ethylene–propylene rubber segments are incorporated as discrete blocks within the polymer chain, improving impact resistance while retaining a relatively high melting point [39]. The base polymer in both cases is isotactic polypropylene (PP-H, homopolymer), whose properties—including a melting temperature of approximately 165 °C, a glass transition near −10 °C, and a semicrystalline morphology favourable for charge trapping—have been reviewed in **Section 2.1.1** [5, p. 325] [7, p. 2]. Blending two grades with different molecular-weight distributions is a common strategy in melt-blowing to optimise the balance between fibre attenuation and web mechanical integrity [8, p. 144S].

Two material variants were prepared. The first set (P−) consists of as-received, untreated fibres. The second set (P+) was produced from a blend containing 30 wt% of H_3PO_4-treated pellets (treated at 100 °C for 24 h) mixed with 70 wt% untreated pellets, as described in **Section 3.2.1**.

The rationale for this treatment is grounded in the charge-trapping framework reviewed in **Section 2.2.2**: H_3PO_4 treatment deepens the trap-energy spectrum of polypropylene by introducing additional localised states at higher energy levels; in melt-blown PP fibres, it has been shown to generate deep traps centred at approximately 1.3 eV, shifting the onset of surface-charge decay upward by approximately 40 °C [14, pp. 33, 36]. An analogous mechanism has been demonstrated for LDPE ferroelectrets, where the same treatment shifted the d_{33} decay curves by 40 K towards higher temperatures [15, pp. 1, 3].

Prior to the experimental programme, both fibre variants were thermally treated at 90 °C for at least 24 h (**Section 3.2.2**) to discharge any residual corona or hydrocharge acquired during production, ensuring electrically neutral starting conditions. Circular samples were then laser-cut from the treated sheets (**Section 3.2.3**).

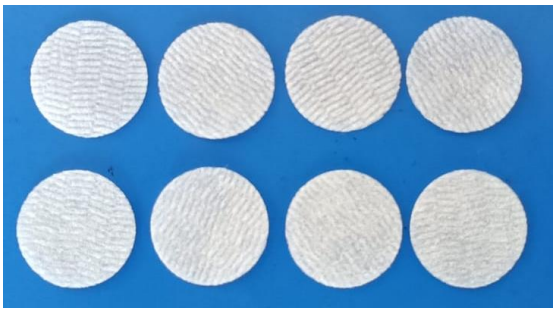

Figure 3.2 *Circular melt-blown PP nonwoven samples (radius 25 mm) used in the DoEs: as-received 50/50 PP-A/PP-B fibres (bottom row) and H_3PO_4-treated fibres (top row).*

Structure of a sample under test. Each sample stack tested in the DoE consists of layers of the same material type (either P− or P+), arranged as follows. The upper and lower layers are equipped with electrodes—circular aluminium foils with a diameter of 15 mm—and are charged via corona at equal voltages in modulus but opposite polarities (the upper layer positively, the lower layer negatively). The electrodes are applied to avoid undesired partial discharges during the transfer of the charged layers from the electric charge section to the d_{33} measurement section. Between the two charged layers, a variable number of intermediate uncharged layers (from zero to three) are interposed; the multi-layer intermediate stacks are fused together at their edges by laser cutting, as described in Section 3.2.3.

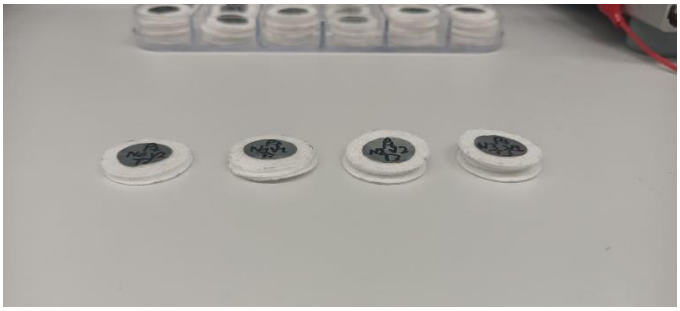

Figure 3.3 *Structure of the sample stacks used in the DoEs, shown from left to right: configurations with zero, one, two, and three intermediate uncharged layers between the corona-charged upper and lower layers. The outermost layers are equipped with aluminium electrodes (diameter 15 mm).*

Standard operating procedure. The electromechanical characterisation of each sample was carried out at room temperature according to the following procedure:

1. *Application of corona charge.* Using the electric charge section, corona charges were applied to the upper and lower layers of the sample for two minutes each. The applied potentials were equal in magnitude but opposite in polarity. The lower layer was charged first, followed by the upper layer.
2. *Verification of the surface potential.* After charging, the Trek 341A electrostatic voltmeter was used to confirm that the intended surface potential had been reached on each layer.
3. *Sample assembly.* The layers were assembled on the B&K Type 8230 force transducer in the following order: lower layer (electrode face down) → intermediate layers → upper layer (electrode face up).
4. *Measurement of d_{33}.* The d_{33} measurement section was used to record the charge and force signals, from which the piezoelectric coefficient was computed.

3.1.3 DoE 2 – Thermal testing and electromechanical characterisation

Having identified the optimal sample configuration via the screening of DoE 1, the second Design of Experiments was designed to investigate the thermal stability of the piezoelectric response.

Objective of the DoE. This DoE aims to characterise how the piezoelectric coefficient d_{33} of the PP fibre samples evolves with increasing temperature. The sample configuration (number of intermediate layers and charging voltage) was fixed to the optimal values identified in DoE 1. Consequently, only two factors were varied: **(i)** P – phosphorus treatment (P−: untreated; P+:

30 wt% blend of H_3PO_4-treated pellets, 100 °C, 24 h); **(ii)** V – charging polarity (V−: default negative voltage; V+: default positive voltage).

Design of the DoE. Two main tests were performed: **(i)** thermally stimulated surface-potential/charge decay (TSCD); **(ii)** temperature dependence of the piezoelectric d_{33} coefficient combined with electromechanical characterisation. The TSCD test required at least five samples per configuration, while the d_{33} vs. temperature test required at least ten samples per material type. The total number of samples is therefore 5 × 2 (P+, P−) × 2 (V+, V−) + 10 × 2 (P+, P−) = 40.

Responses to the DoE. The desired outputs are three graphs: **(i)** a TSCD plot showing the normalised surface potential (p.u.) as a function of temperature for four configurations (P−/V−, P−/V+, P+/V−, P+/V+); **(ii)** a d_{33} vs. temperature plot showing the piezoelectric coefficient (in pC/N) and the residual percentage of the initial d_{33} at each isothermal step, for both P− and P+ samples.

Instrumentation and experimental setup. The work area is divided into three sections, as illustrated in the block diagram of **Figure 3.4**. The electric charge section is identical to that of DoE 1 (**Figure 3.1a**). The d_{33} measurement section is also identical, with the exception that the Burster 8435-5200 force transducer replaces the B&K Type 8230, as it supports both dynamic and static force measurements (**Section 3.1.1**). The thermal testing section is specific to DoE 2 and includes the Trek 341A electrostatic voltmeter (for surface-potential acquisition during TSCD) and the G. MAIER R12/SSR/PT100/3300/230 temperature regulator (for controlled heating of the sample).

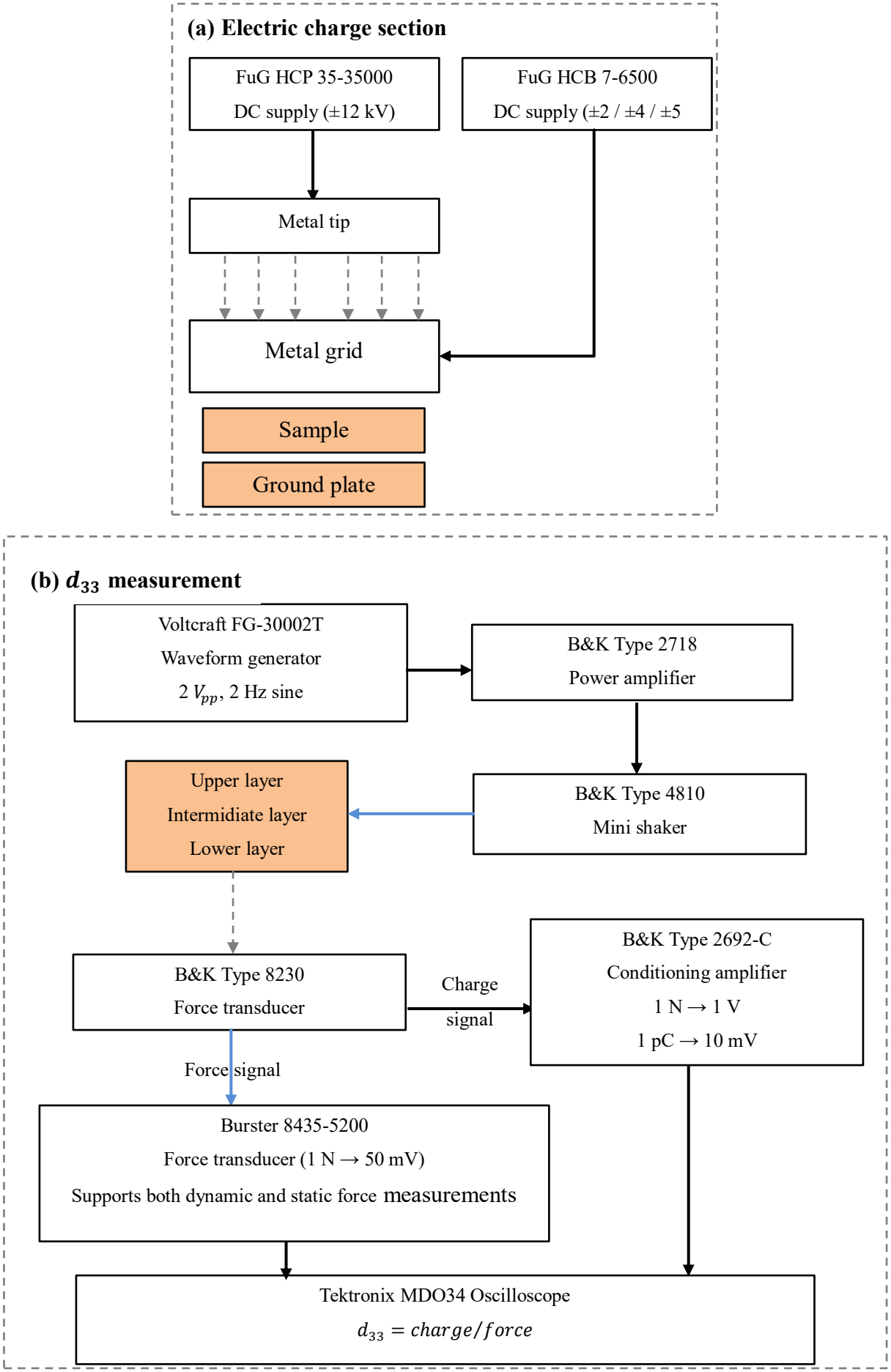
(a) Electric charge section
FuG HCP 35-35000
DC supply (±12 kV)
FuG HCB 7-6500
DC supply (±2 / ±4 / ±5
Metal tip
Metal grid
Sample
Ground plate
(b) d_{33} measurement
Voltcraft FG-30002T
Waveform generator
2 V_{pp}, 2 Hz sine
B&K Type 2718
Power amplifier
Upper layer
Intermidiate layer
Lower layer
B&K Type 4810
Mini shaker
B&K Type 8230
Force transducer
Charge
signal
B&K Type 2692-C
Conditioning amplifier
1 N → 1 V
1 pC → 10 mV
Force signal
Burster 8435-5200
Force transducer (1 N → 50 mV)
Supports both dynamic and static force measurements
Tektronix MDO34 Oscilloscope
$d_{33} = charge/force$

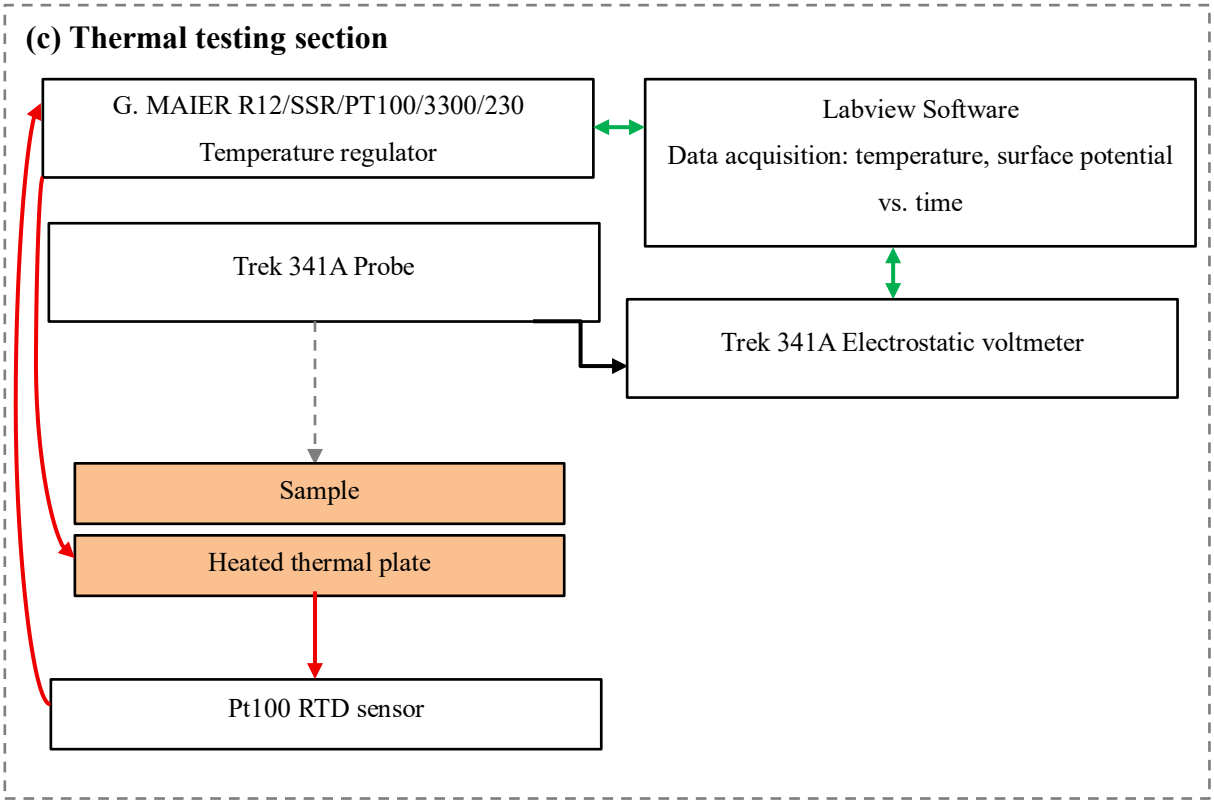

Figure 3.4 *Block diagram of the experimental setup used for DoE 2, comprising three functional sections: (a) electric charge section (which is identical to DoE 1 (Figure 3.1a)), (b) d_{33} measurement section (which is identical to DoE 1 (Figure 3.1b), except for the usage of a Burster 8435-5200 force transducer), (c) thermal testing section. The signal flow is indicated by black arrows (electrical signal transferred through cables), blue arrows (mechanical signal), dotted grey arrows (electrical signal transferred through air), red arrows (thermal signal) and green arrows (digital signal).*

Structure of the samples under test. Two types of samples were used, depending on the test: For the TSCD test, individual single-layer samples (equivalent to the upper or lower layers used in DoE 1) were employed. The choice of thin, single-layer specimens was motivated by the need to minimise the temperature gradient across the sample thickness during the controlled heating ramp: if the material is too thick, an excessive ramp rate can produce a temperature gradient that causes the sample to heat faster than intended—a condition that would compromise the accuracy of the TSCD characterisation.

For the d_{33}vs. temperature test, the multi-layer sample stacks described in **Section 3.1.2** were used, with the intermediate-layer configuration fixed to the optimum identified in DoE 1.

Standard operating procedure. The three main procedures are detailed below.

1. Electromechanical characterisation. This procedure is identical to that described for DoE 1 (Section 3.1.2) and is used both as a standalone measurement and as a sub-step within the d_{33} vs. temperature protocol.

2. Thermally stimulated surface-potential/charge decay (TSCD). This measurement characterises the variation of the surface potential—and hence the surface charge—as a function of temperature. As the temperature increases, the trapped charges are progressively released from their localised states (as described in **Section 2.2.2**), causing the surface potential to decrease until it vanishes entirely near the melting temperature of PP. The procedure is as follows:

- *Corona charging:* A single layer is charged using the electric charge section, at one of the two preset polarities (V+ or V−), for two minutes.
- *Software setup:* A LabView-based data acquisition programme, pre-existing at the TSC, is configured with a temperature ramp of 3 °C/min and a maximum temperature of 200 °C. The software simultaneously records the surface potential (via the Trek 341A) and the plate temperature (via the Pt100 sensor) as a function of time.
- *Heating and measurement:* The sample charged is placed on the heated plate, under the Trek 341A probe, and the programme is started. The surface potential and temperature are logged continuously until the end of the ramp.

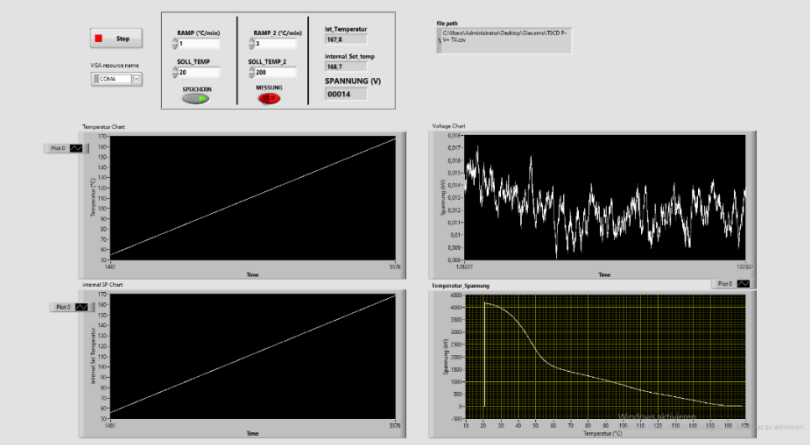

Figure 3.5 *User interface of the LabView-based data acquisition software used in DoE 2 for TSCD and thermal d_{33} characterisation. The main panels display, from top-left to bottom-right: ramp parameters (ramp rate, target temperature, interval), real-time temperature chart, real-time surface potential chart, internal set-point chart, and the temperature–surface potential correlation plot.*

3. Temperature dependence of the piezoelectric d_{33} coefficient. This procedure evaluates how the d_{33} coefficient evolves with increasing temperature. It is structured as follows:

- *Corona charging and sample assembly:* The multi-layer sample is prepared as described in the electromechanical characterisation procedure.

- *Software setup:* The same LabView software is used but configured with faster thermal ramps (20 °C/min) to approximate an isothermal step model. Five steps are applied: 20 °C, 40 °C, 60 °C, 80 °C, and 100 °C, each held for one hour.
- *Heating and measurement:* At each temperature step, the sample is heated on the plate for one hour. After each isothermal hold, the sample is returned to room temperature, and an electromechanical characterisation is performed (as described in **Section 3.1.2**). This cycle is repeated for all five temperature steps, producing a curve of d_{33}vs. temperature.

3.1.4 Microscopic Characterisation of the Materials (OM)

In addition to the electromechanical and thermal characterisations described above, two complementary techniques were employed to characterise the morphology and mechanical properties of the tested materials.

Microscopic characterisation of the melt-blown PP nonwovens is essential for analysing the fibre morphology and highlighting the visual differences between untreated and H_3PO_4-treated PP electrets, as well as for quantifying the fibre diameter distribution. The instrument used for this purpose was the KEYENCE VHX-5000, a digital microscope that captures high-resolution colour images using a 1/1.8-inch CMOS image sensor and high-brightness LED illumination. It combines optical imaging with software-based functions such as 16-bit HDR, focus stacking (3D depth composition), and image stitching to support extended-depth and wide-area observation. Its key specifications include a sensor resolution of 1600 × 1200 pixels, continuously adjustable magnification from 20× to 2000× via two rotating lenses, and an operating range of 100–240 VAC (50/60 Hz), 280 VA [40, pp. 1–2].

Using 3D depth composition at 1000× magnification, ten micrographs were captured for each material type (untreated and H_3PO_4-treated). Twenty fibre-diameter measurements were performed per micrograph, yielding a total of one hundred measurements per material type. These data were used to construct statistical distribution histograms with fitted Gaussian curves for the fibre diameters of both PP variants.

3.1.5 Surface hardness characterisation

The morphological characterisation of the samples was completed by measuring their surface hardness using the Heinrich Bareiss DIGI TEST II, a modular digital durometer for indentation hardness testing (resistance to elastic deformation) of polymers and elastomers via interchangeable Shore/IRHD measuring units. Its key specifications include support for

standardised hardness scales spanning Shore A, Shore D, and additional variants (Micro A, A0, B, 0, C, Micro D, D0, 00, 000, 000S, E, AM, M), plus IRHD (Micro, Normal, Hard, Low) and VLRH for very soft elastomers; digital measurement features with 0.1-division resolution, selectable measuring time from 1 to 99 s, and data interfaces via USB and RS-232; and a modular plug-and-play concept supporting more than 20 interchangeable methods with a changeover time of ≤10 s [41, pp. 3–4, 17–19].

Surface hardness characterisation was performed using the Shore A scale on both material types (as received and H_3PO_4treated). The measurements were carried out on a complete reference sample used in DoE 2 and on its constituent parts—namely the individual upper/lower layer and the three-level intermediate stack—both with and without the aluminium electrodes. This systematic characterisation provides information on the stiffness of each component and of the complete stack, which is relevant to the interpretation of the d_{33} measurements, as discussed in **Chapter 5**.

3.2 Processing of PP fibre sheets

Before the PP fibre samples could be subjected to the DoEs described above, several preparatory processing steps were required. This section describes the chemical treatment with phosphorus (**Section 3.2.1**), the thermal discharge treatment (**Section 3.2.2**), and the laser cutting of individual and fused layers (**Section 3.2.3**). Note that the production of the PP fibre sheets via melt-blowing is not described here, as this process has already been reviewed in **Section 2.1.2**.

3.2.1 Chemical treatment with phosphorus for PP fibre sheets

As described in **Sections 3.1.2** and **3.1.3**, the two material variants are distinguished by the presence or absence of a chemical treatment with phosphorus. For PP fibres, this treatment is applied upstream to the pellets used as feedstock for the melt-blowing process, so that the modified chemical characteristics are already incorporated into the finished nonwoven product. The treatment consists of immersing the PP pellets in orthophosphoric acid (H_3PO_4) for 24 hours at 100 °C, followed by thorough rinsing with deionised water. The treated pellets (30 wt%) were then blended with untreated pellets (70 wt%) before being fed into the melt-blow extruder. The purpose of this treatment is to improve the ability of the material to trap electric charges at its surface and within its bulk—a fundamental requirement for enhancing the piezoelectric response of ferroelectrets. Pellets modified in such a way are later added to a non-treated PP in concentration of 30 wt% directly in the melt-blow extruder. As reviewed in

Section 2.2.2, the H_3PO_4treatment introduces additional deep trap states in the polymer energy spectrum, shifting the onset of thermally activated charge decay towards higher temperatures [14, pp. 33, 36] [15, pp. 1, 3].

3.2.2 Thermal treatment of PP fibre sheets

As mentioned in **Section 3.1.2**, the PP fibre sheets used in this work were originally subjected to corona charging or hydrocharging during their industrial production. However, the presence of residual surface or bulk charges prior to the experimental programme would alter the d_{33} measurements, since the baseline electrical state of the samples would be undefined. To ensure electrically neutral starting conditions, a thermal treatment was applied to the PP fibre sheets: they were heated to 90 °C for at least 24 hours using a PRÄZITHERM high-temperature hot plate.

This laboratory heating system is designed for continuous operation up to 600 °C, featuring a titanium heating plate (280 mm × 200 mm overall, with a stated constant-temperature area of 230 mm × 160 mm) and either a PID temperature controller or a programmable ramp controller for time–temperature profiles. It reaches 600 °C in approximately 20 min and operates from 230 V (50–60 Hz) with a rated power of 2000 W (PZ 28-3TD, with cover) or 2200 W (PZ 28-3T, without cover) [42, pp. 1–2].

3.2.3 Laser cutting of PP layers

Individual layers and fused multi-layer intermediate stacks were prepared from the thermally treated PP fibre sheets using a Laserbox Pro von Makeblock, an enclosed CO_2 laser cutting and engraving system. The machine operates within a protected working chamber and includes a lid safety interlock that automatically halts operation if the chamber is opened [43, p. 4]. Its key parameters are a working temperature range of 5–25 °C, maximum cutting dimensions of 500 mm (L) × 300 mm (W) × 22 mm (T), and connectivity via USB, Ethernet, or Wi-Fi through dedicated LaserBox software [43, pp. 4, 9, 18]. The software also integrates a built-in camera for image extraction and positioning workflows [43, p. 17]. The user interface allows the operator to define the cutting mask geometry, the material type (with the option to catalogue custom profiles), the material thickness, the laser power (0–100%), and the cutting speed (0–80 mm/s).

Cutting of individual layers. Circular samples with a radius of 25 mm were cut from the thermally treated PP fibre sheets using the mask shown in Figure 3.6 and the following settings: material—not defined, 1 mm thickness; power—20%; speed—5 mm/s.

Fusion of intermediate layers. To join two or three layers of PP fibres along the edges, a plexiglas holder was first fabricated to house the individual layers during the fusion step. A 50 × 50 mm square block with a central circular aperture (radius 25 mm) was cut from a plexiglas sheet using the mask shown in **Figure 3.7** (left), with the following settings: material—acrylic, 3 mm thickness; power—100%; speed—6 mm/s. The finished holder (**Figure 3.7**, right) was glued to the base of the metal grid inside the Laserbox chamber, so that the PP layers could be placed inside the aperture and fused at the edges. The fusion settings were material—not defined, 2 mm thickness (for two-layer stacks) or 3 mm (for three-layer stacks); power—30% (two layers) or 35% (three layers); speed—5 mm/s. Examples of the resulting one-, two-, and three-layer intermediate stacks are shown in **Figure 3.8**.

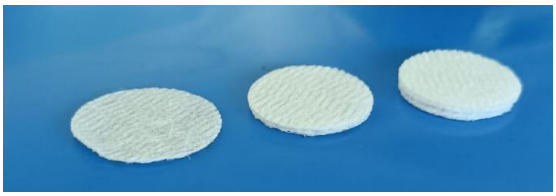

Figure 3.6 *Examples of fused intermediate-layer stacks: from left to right, single-layer, two-layer, and three-layer configurations. The edge fusion was performed at 30–35% laser power and 5 mm/s speed.*

4. EXPERIMENTAL RESULTS

This chapter presents the experimental results obtained from the characterisation programme described in **Chapter 3**. The outputs of the two DoEs are reported first—the process–factor screening (**Section 4.1**) and the thermal testing combined with electromechanical characterisation (**Section 4.2**)—followed by the morphological and structural characterisation of the melt-blown PP nonwovens (**Section 4.3**). The data are presented together with a statistical analysis of the factorial design (ANOVA, main effect plots, Pareto chart) to quantify the main trends; a detailed physical discussion and comparison with the existing literature is deferred to **Chapter 5**.

4.1 Outputs of DoE 1 – Process-factor screening of PP fibres

After performing the electromechanical characterisation for all 24 configurations, the measured d_{33} values are summarised in **Table 4.1**. The following key applies: P – phosphorus treatment (P−: untreated; P+: 30 wt% blend of H_3PO_4-treated pellets, 100 °C, 24 h); N – number of intermediate layers (N0: 0; N1: 1; N2: 2; N3: 3); V – charging voltage applied to the upper and lower layers (V1: ±2 kV; V2: ±4 kV; V3: ±5 kV); $d_{33,avg}$ – arithmetic mean of d_{33} over the three repetitions. The highest $d_{33,avg}$ for untreated samples is highlighted in yellow, and the highest for chemically treated samples is highlighted in blue.

Table 4.1 *Piezoelectric coefficient d_{33} measured for all 24 configurations of DoE 1 (2 phosphorus treatments × 4 intermediate-layer counts × 3 charging voltages). Each configuration was tested on three independent samples. The highest $d_{33,avg}$ for untreated (P−) and treated (P+) samples is highlighted in yellow and light blue, respectively.*

Configuration	d_{33} avg (pC/N)	d_{33} (pC/N) TEST 1	d_{33} (pC/N) TEST 2	d_{33} (pC/N) TEST 3
P-; N0; V1	60.3	80.0	50.4	50.4
P-; N0; V2	58.0	88.0	25.0	61.0
P-; N0; V3	74.7	115.0	24.0	85.0
P-; N1; V1	12.7	24.0	8.0	6.0
P-; N1; V2	49.3	88.0	22.0	38.0
P-; N1; V3	62.7	42.0	38.0	108.0
P-; N2; V1	48.0	24.0	47.0	73.0
P-; N2; V2	103.8	150.0	50.3	111.0
P-; N2; V3	80.7	74.0	79.0	89.0
P-; N3; V1	18.7	15.0	17.0	24.0
P-; N3; V2	69.7	83.0	54.0	72.0
P-; N3; V3	107.7	89.0	126.0	108.0

Configuration	d_{33} avg (pC/N)	d_{33} (pC/N) TEST 1	d_{33} (pC/N) TEST 2	d_{33} (pC/N) TEST 3
P+; N0; V1	2.1	2.2	1.9	2.2
P+; N0; V2	13.0	11.0	12.0	16.0
P+; N0; V3	20.3	27.0	15.0	19.0
P+; N1; V1	8.2	6.0	17.0	1.6
P+; N1; V2	9.7	8.7	10.5	9.9
P+; N1; V3	10.3	11.4	10.0	9.4
P+; N2; V1	9.5	15.2	6.4	6.8
P+; N2; V2	26.7	11.0	27.4	41.6
P+; N2; V3	27.5	36.0	31.6	15
P+; N3; V1	3.5	3.6	4.7	2.3
P+; N3; V2	19.4	22.6	25.4	10.2
P+; N3; V3	29.9	23.8	29.8	36.0

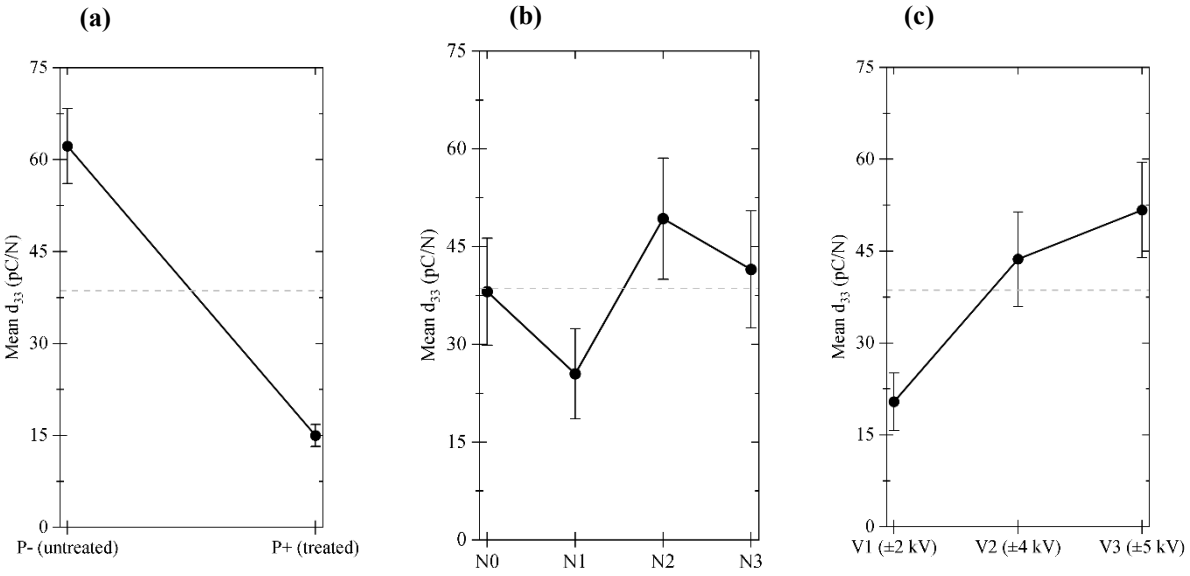

Figure 4.1. *Main effect plot for d_{33} as a function of the three DoE 1 factors: (a) phosphorus treatment (P), (b) number of intermediate layers (N), and (c) charging voltage (V). Each point represents the grand mean of d_{33} at the corresponding factor level; error bars indicate the standard error of the mean. The dashed grey line marks the overall grand mean (38.6 pC/N). Data from 72 individual measurements (**Table 4.1**) [38, sec. 5.5.9.3].*

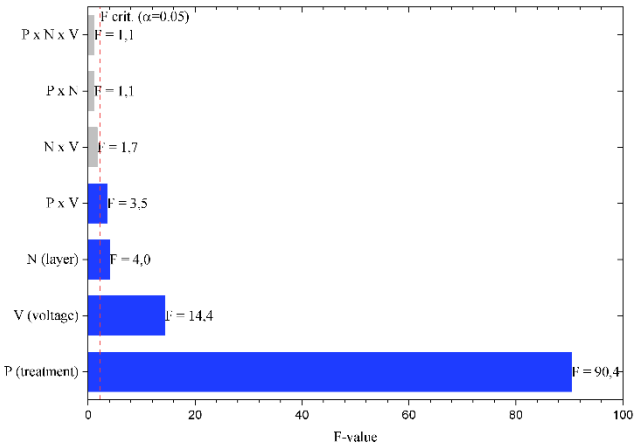

Figure 4.2. *Pareto chart of standardised effects (F-values) from the full factorial ANOVA on d_{33} (**Table 4.1**). Blue bars indicate statistically significant effects ($p < 0.05$); grey bars indicate non-significant effects. The dashed red line marks the critical F-value at $\alpha = 0.05$ for the highest-order interaction term ($F_{6,48} = 2.29$); effects with fewer degrees of freedom have higher individual thresholds but all significant effects exceed their respective critical values [38, sec. 5.5.9.7].*

To quantify the relative importance of each factor on the piezoelectric response, a full factorial analysis of variance (ANOVA) was performed on the 72 individual d_{33} measurements [38, sec. 5.3.3.3, 5.5.9.3, 5.5.9.7]. The Pareto chart of standardised effects (**Figure 4.2**) and the main effect plot (**Figure 4.1**) summarise the results.

The phosphorus treatment (P) is by far the dominant factor, accounting for 43.7% of the total variation ($F = 90.4$, $p < 0.001$): untreated samples yield a mean d_{33} of 62.2 pC/N versus 15.0 pC/N for treated samples, a ratio of approximately 4:1. The charging voltage (V) is the second most influential factor (13.9% of variation, $F = 14.4$, $p < 0.001$), with d_{33} increasing monotonically from V1 (20.4 pC/N) to V3 (51.7 pC/N). The number of intermediate layers (N) has a statistically significant but smaller effect (5.8%, $F = 4.0$, $p = 0.013$), with a non-monotonic pattern: d_{33} decreases from N0 to N1, then increases for N2 and N3. A significant P × V interaction ($F = 3.5$, $p = 0.039$) indicates that the voltage effect is more pronounced for untreated than for treated samples. The remaining interactions (P × N, N × V, P × N × V) are not statistically significant.

The best-performing configuration for untreated samples is P−; N3; V3, with a $d_{33,avg}$ of 107.7 pC/N; for treated samples, the highest value is reached by P+; N3; V3 at 29.9 pC/N. The residual error accounts for 23.2% of the total variation, consistent with the considerable inter-sample variability observed in certain configurations (e.g., P−; N0; V2 ranges from 25 to 88 pC/N across the three repetitions). Despite this scatter, the ANOVA confirms that the main effects of P and V are highly significant ($p < 0.001$), indicating that the overall ranking of

configurations is robust. The N3; V3 configuration was therefore selected as the basis for DoE 2.

Representative oscilloscope traces for the two optimal configurations are shown in **Figures 4.3 and 4.4**. In both figures, the yellow trace (CH2) represents the charge signal, and the blue trace (CH1) represents the applied force signal. The conversion factors set on the conditioning amplifier are: 1 N → 1 V (force) and 1 pC → 10 mV (charge).

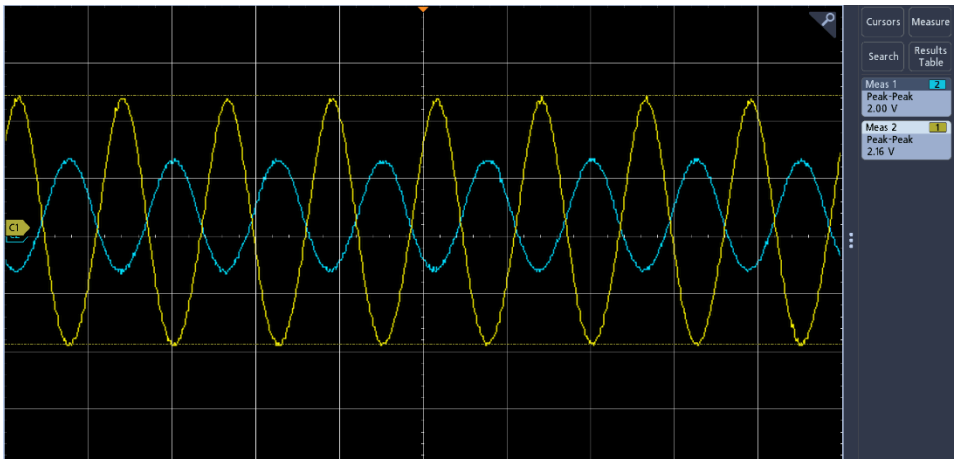

Figure 4.3 *Oscilloscope traces for the P−; N3; V3 configuration (TEST 3): charge output (yellow, CH2, peak-to-peak 2.6 V ≈ 260 pC) and applied sinusoidal force (blue, CH1, peak-to-peak 2.00 V ≈ 2.00 N) at 2 Hz. The resulting piezoelectric coefficient is* $d_{33} \approx 130\ pC/N$.

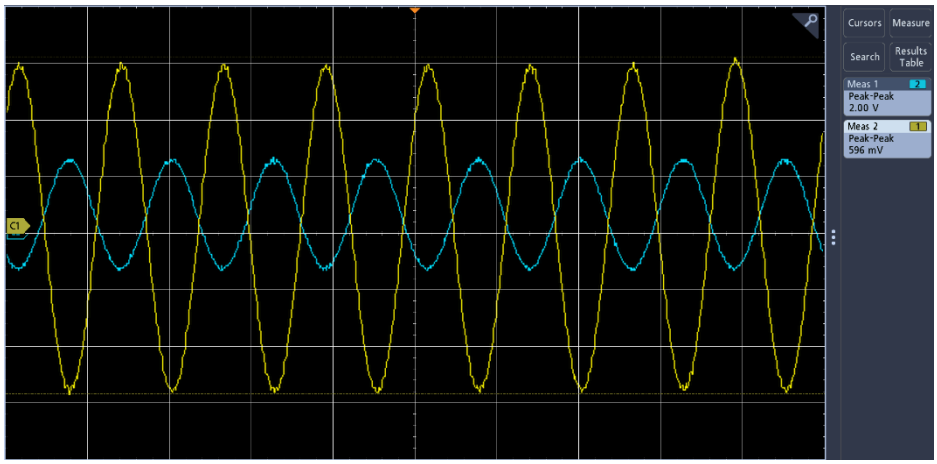

Figure 4.4 *Oscilloscope traces for the P+; N3; V3 configuration (TEST 2): charge output (yellow, peak-to-peak 596 mV ≈ 59.6 pC) and applied force (blue, peak-to-peak 2.00 V ≈ 2.00 N). The resulting piezoelectric coefficient is* $d_{33} \approx 29.8\ \ pC/N$.

4.2 Outputs of DoE 2 – Thermal testing and electromechanical characterisation

4.2.1 Thermally stimulated surface-potential decay

Following the TSCD procedure described in **Section 3.1.3**, the normalised surface-potential decay curves shown in **Figure 4.5** were obtained for four sample configurations. The explanatory key is :P – phosphorus treatment (P−: untreated; P+: 30 wt% blend of H_3PO_4-treated pellets, 100 °C, 24 h); V – charging polarity (V−: −5 kV; V+: +5 kV).

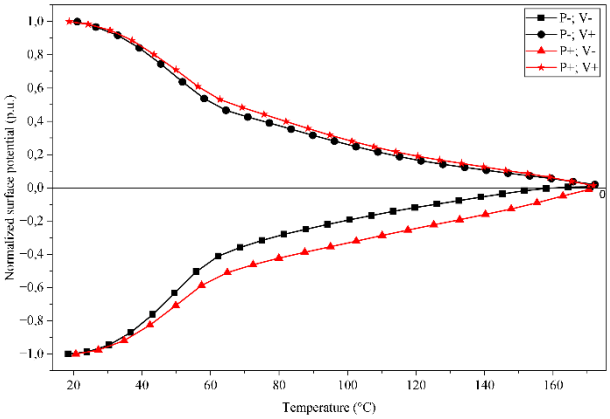

Figure 4.5 *Thermally stimulated surface-potential decay of corona-charged melt-blown PP nonwovens. Normalised surface potential (p.u.) vs. temperature (°C) for four configurations: as-received (P−) and H_3PO_4-treated (P+) samples charged to −5 kV (V−) and +5 kV (V+). Heating rate: 3 °C/min.*

The TSCD curves reveal several noteworthy features. The charge polarity influences the decay profile: negatively charged samples (V−) generally retain a higher fraction of their initial surface potential at elevated temperatures than positively charged samples (V+), consistent with the known asymmetry of trap states for positive and negative carriers in polypropylene. For the as-received samples (P−), a pronounced decay begins near 60 °C and the surface potential approaches zero by approximately 120 °C. The H_3PO_4-treated samples (P+) exhibit a notably extended charge-retention plateau: the onset of significant decay is shifted upward by approximately 20–30 °C compared with the untreated material, and a residual surface potential persists up to approximately 140–150 °C. This behaviour is consistent with the deeper trap states introduced by the phosphorus treatment, as discussed in **Section 2.2.2** [14, pp. 33, 36].

4.2.2 Temperature dependence of the piezoelectric coefficient d_{33}

The temperature dependence of the d_{33} coefficient was measured using the isothermal step protocol described in **Section 3.1.3**, producing the curves shown in **Figure 4.6**.

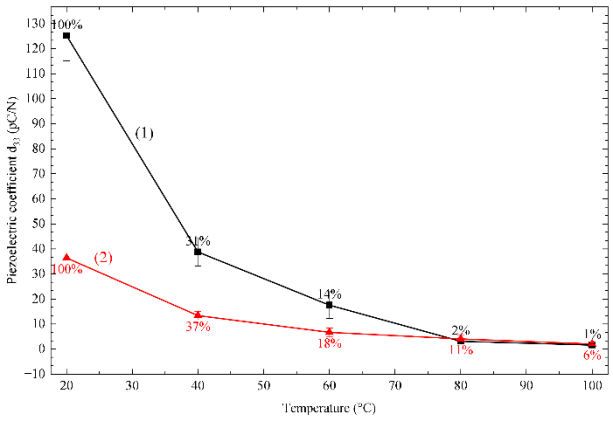

Figure 4.6 *Temperature dependence of the piezoelectric coefficient d_{33} in melt-blown PP nonwovens: (1) as-received samples; (2) samples treated with H_3PO_4. The percentages indicate the residual fraction of the initial d_{33} at each isothermal step (20, 40, 60, 80, and 100 °C, 1 h each). Error bars represent the standard deviation across the tested samples.*

The as-received samples (curve 1) start from a higher initial d_{33} (approximately 130 pC/N at 20 °C) but exhibit a steep decline with increasing temperature: the residual d_{33} drops to approximately 38% of its initial value after one hour at 60 °C and falls below 2% at 100 °C. The H_3PO_4-treated samples (curve 2) start from a lower initial d_{33} (approximately 30 pC/N at 20 °C) but show improved relative thermal stability: they retain approximately 57% of their initial value after one hour at 40 °C and approximately 14% at 60 °C. At 80 °C and above, both material types have lost most of their piezoelectric response, with the treated samples retaining approximately 11% at 80 °C compared with 2% for the untreated ones.

These results indicate a clear trade-off between absolute piezoelectric performance (higher for untreated samples) and thermal stability of the response (improved for treated samples). A detailed interpretation of this trade-off, including a comparison with literature values for PP ferroelectrets, is provided in **Chapter 5**.

4.3 Morphological and structural characterisation

4.3.1 Microscopic Characterisation of the Materials (OM)

As described in **Section 3.1.4**, the fibre morphology of the melt-blown PP nonwovens was characterised by optical microscopy at 1000× magnification. The results are presented in **Figure 4.7**, which shows representative micrographs alongside the fibre-diameter histograms and fitted Gaussian distributions for both material types.

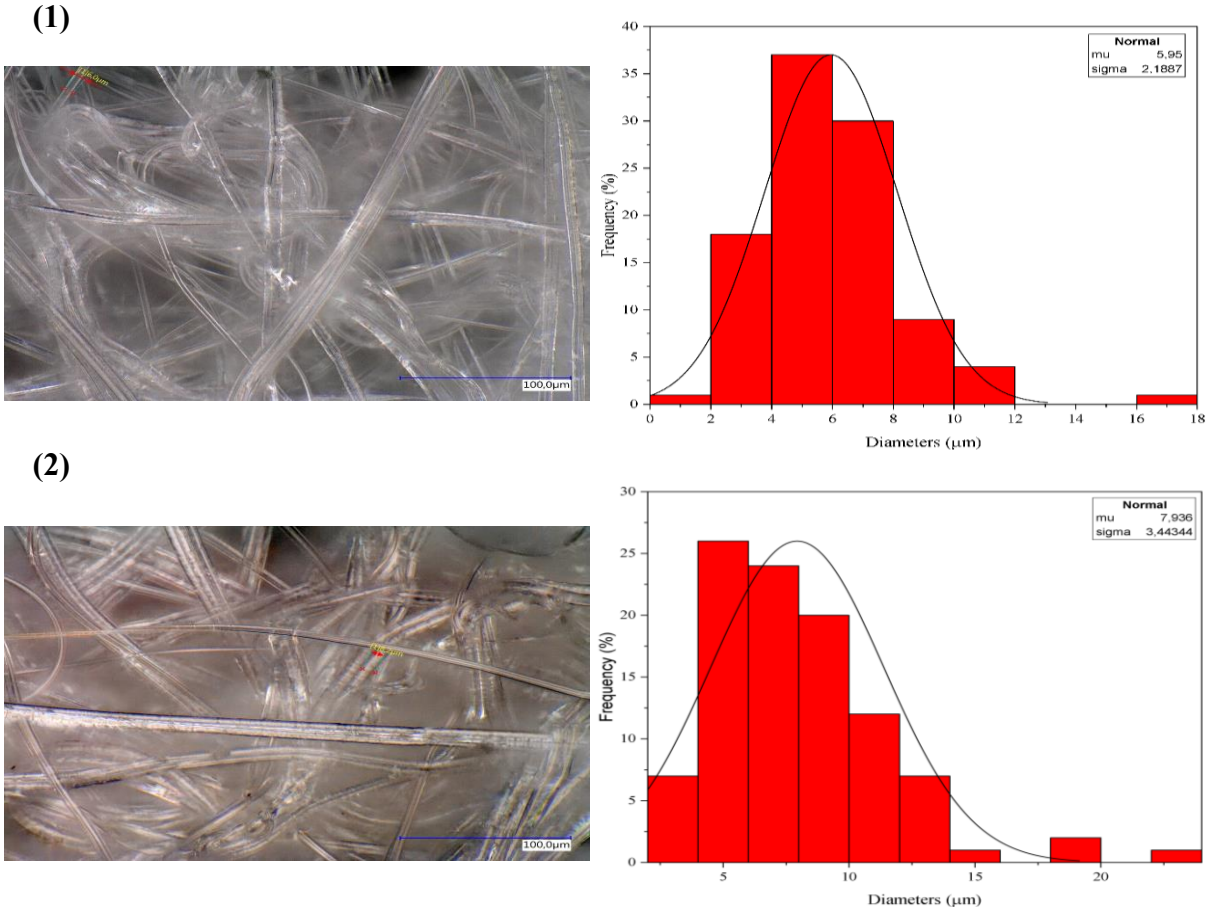

Figure 4.7 *Optical microscopy (OM) characterisation of melt-blown PP nonwovens at 1000× magnification: (1) as-received fibres (mean diameter μ = 5.95 µm, standard deviation σ = 2.19 µm); (2) H_3PO_4-treated fibres (μ = 7.94 µm, σ = 3.44 µm). Left column: representative micrographs with 100 µm scale bar; right column: fibre-diameter histograms (100 measurements each) with fitted Gaussian distributions.*

The as-received fibres exhibit a mean diameter of 5.95 µm with a standard deviation of 2.19 µm, while the H_3PO_4-treated fibres show a larger mean diameter of 7.94 µm and a broader distribution (σ = 3.44 µm). This morphological difference—an increase of approximately 33% in mean fibre diameter and 57% in distribution width—may reflect the effect of the chemical treatment on the melt rheology of the PP pellets during the melt-blowing process: the presence of residual phosphoric acid or phosphate groups on the pellet surface could alter the melt viscosity, leading to reduced fibre attenuation and, consequently, thicker fibres with greater diameter variability. A more detailed discussion of this observation is provided in **Chapter 5**.

4.3.2 Surface hardness testing

The surface hardness of the melt-blown PP nonwoven components was measured using the Shore A scale on the Bareiss DIGI TEST II durometer, as described in **Section 3.1.5**. The results

are summarised in **Table 4.2**, along with the corresponding thickness measurements. The Shore A values were converted to an estimated Young's modulus using the following empirical relationship [44]:

$$E(MPa) = 10^{(0.0235 \cdot S - 0.6403)} \quad (4.1)$$

where S is the Shore A value (dimensionless).

Table 4.2 *Measured Shore A hardness and thickness of the melt-blown PP nonwoven components and assembled stacks for as-received and H_3PO_4-treated samples. The Young's modulus is estimated via the empirical relation of Eq. (4.1).*

As received melt-blown PP nonwovens	**Shore A / E (MPa)**	**Thickness (mm)**
Single layer	32.5 / 1.33	0.51
3-level intermediate layers	34 / 1.44	1.09
Entire stack (without electrodes)	25.9 / 0.93	2.12
Entire stack (with electrodes)	71.6 / 11.02	2.75
Melt-blown PP nonwovens treated with H_3PO_4	**Shore A/E (MPa)**	**Thickness (mm)**
Single layer	38 / 1.79	0.44
3-level intermediate layers	31.1 / 1.23	1.74
Entire stack (without electrodes)	30.6 / 1.20	2.5
Entire stack (with electrodes)	73.3 / 12.09	3.89

The results show that the individual layers are relatively soft (Shore A ≈ 32–38), with the H_3PO_4-treated single layers exhibiting a slightly higher hardness (38 vs. 32.5 Shore A) despite being thinner (0.44 vs. 0.51 mm). The assembled stacks without electrodes remain in the same softness range (Shore A ≈ 26–31), but the addition of the aluminium electrodes dramatically increases the measured hardness (Shore A ≈ 72–73) and the estimated Young's modulus by nearly an order of magnitude (from ≈1 MPa to ≈11–12 MPa). This large increase reflects the much higher stiffness of the aluminium foil relative to the nonwoven polymer layers and indicates that, during the d_{33} measurement, the electrodes dominate the mechanical response of the outer surfaces of the stack. The implications of this observation for the interpretation of the d_{33}values are discussed in **Chapter 5**.

5. DISCUSSION

This chapter aims to discuss and argue the experimental results shown in **Chapter 4**, considering the theoretical notions expressed in **Chapter 2**. Starting from an attempt at a physical interpretation of the experimental results (**Section 5.1**) and a comparison with the scientific literature relevant to the topic (**Section 5.2**), we then proceed to outline the strengths (**Section 5.3**) and weaknesses (**Section 5.4**) of the thesis, concluding with suggestions for future research (**Section 5.5**).

5.1 Physical interpretation of experimental results

Considering what has been discussed in **Chapter 4**, this paragraph attempts to provide a physical interpretation of the phenomena observed considering the theory outlined in **Chapter 2**. Where there is no single interpretation of the observed phenomenon, interpretative hypotheses are put forward, which may lead to suggestions for future work in **Section 5.5**.

5.1.1 Interpretation of DoE 1 results (effect of V, N, P on d_{33})

Effect of charging voltage on d_{33}. As confirmed by the ANOVA reported in **Section 4.1** ($F = 14.4$, $p < 0.001$; 13.9% of total variation), the charging voltage is the second most influential factor on d_{33} after the phosphorus treatment. For both as-received PP nonwovens and H_3PO_4-treated PP nonwovens, the average piezoelectric coefficient d_{33} increases with increasing voltage V with which the corona discharge was performed on the upper and lower layers. This is consistent with theory, especially in **Section 2.2.1** (**Eq. 2.1**) regarding Schottky (thermionic) emission, in **Section 2.3.1** regarding the operative definition of d_{33} used for quasi-static (Berlincourt) method and in **Section 2.3.2** (**Fig. 2.4**), where dielectric barrier discharges (DBD) within the cavities may also contribute to the charging process, although the samples were charged directly in corona.

Looking at the theory mentioned above, **Eq. 2.1** is useful for understanding how the injection current derived from the corona discharge grows exponentially with the electric field—at a fixed temperature. Therefore, having a higher voltage leads to an increase in the number of charge carriers injected and, consequently, in the surface charge captured in the cavities of the PP nonwovens. Furthermore, the operational definition $d_{33} = \Delta Q / \Delta F$ used for the quasi-static method of measuring the piezoelectric coefficient supports the observations made above. In fact, for the same applied force, more charge trapped in the cavities implies a greater variation

in charge under deformation and therefore a higher d_{33}. Additionally, it should be noted that dielectric barrier discharges (DBD) within the cavities may also play a role at higher voltages. When the local field exceeds the Paschen threshold, the gas within the cavities can be ionised, depositing additional charge carriers on the cavity walls and generating macroscopic dipoles. However, since the samples in this work were charged directly via corona discharge, the relative contribution of cavity-internal DBD remains uncertain and may be secondary to the direct charge injection mechanism. This dependence of d_{33} on the applied voltage through the DBD mechanism is consistent with the analysis provided by Moreira et al. [22, p. 4] and with the detailed review by Qiu [45, pp. 011101-4–5].

The maximum limit imposed in **Section 3.1.2** on the voltage to be applied during corona discharge must also be discussed. This limit was chosen both in reference to the physical limit of voltage that can be generated by the FuG HCB 7–6500 bipolar supplier (0 to ±6500 V) and because it was decided to keep the position of the ground plate on which the samples rested fixed. This limited the maximum voltage that could be applied during testing but still allowed DBD to be performed at voltages that had not been previously tested on PP nonwovens.

Effect of intermediate layers on d_{33}. The ANOVA confirms that the number of intermediate layers has a statistically significant but modest effect on d_{33} (F = 4.0, p = 0.013; 5.8% of total variation). As visible in the main effects plot (**Figure 4.1**), the response follows a non-monotonic pattern: d_{33} decreases from N0 to N1, then increases for N2 and N3. This behaviour partly reflects what is expressed in the theoretical part, in **Section 2.3.1** (**Eq. 2.6b**) regarding the constitutive equation of piezoelectricity on deformation S, and in **Section 2.3.2** regarding the relationship between cavity deformation and distance between charges.

Going into the theory, **Eq. 2.6b** shows that, with greater elastic compliance s, there is greater deformation S under the same force, resulting in a higher charge signal. Furthermore, in accordance with **Section 2.3.2**, the deformation of the cavities changes the distance between the trapped charges, causing a variation in surface charge and generating the piezoelectric effect. The positive correlation between mechanical compliance and piezoelectric response in multilayer ferroelectrets has been documented by Qiu et al. [46, p. 2341009-14], and Assagra et al. demonstrated the tunability of the piezoelectric response through multilayer stacking in 3D-printed PP [23, pp. 1668, 1671].

Considering this theoretical evidence, it is still not easy to understand why the piezoelectric coefficient d_{33} measured without intermediate layers is greater than that measured with a single intermediate layer. This phenomenon may indicate that the addition of a single layer does not

result in a sufficient reduction in elastic stiffness and may only hinder the interaction between dipoles, which is maximised in the configuration without intermediate layers. Consequently, the addition of more than one intermediate layer can overcome the problem of lack of interaction between dipoles of opposite charge, while still ensuring an increase in d_{33}. Finally, the possible effect on the elastic response of the sample caused by the presence of the aluminium electrode in the upper and lower layers should not be ruled out.

In order to further understand this phenomenon, it is therefore necessary to also take into account the results of **Table 4.2**, from which it can be deduced that the stack formed by the upper, lower and intermediate layers actually has a lower Young's modulus than that of the single layer, but the addition of the aluminium electrode significantly increases the Young's modulus of the entire stack. This raises potential complications that have been added by the choice of that specific electrode, but this will be further explored in **Section 5.1.3**.

Effect of H_3PO_4 treatment on d_{33} at room temperature. The ANOVA identifies the phosphorus treatment as by far the dominant factor ($F = 90.4$, $p < 0.001$), accounting alone for 43.7% of the total variation — more than three times the contribution of voltage and six times that of intermediate layers. **Table 4.1** confirms that the d_{33} of H_3PO_4-treated PP nonwovens is approximately 3–4 times lower than that of as-received PP nonwovens. This phenomenon cannot be explained without considering the nature of the samples and the relationship between morphology and the piezoelectric coefficient d_{33}.

As stated in **Section 2.1.2** regarding the melt-blowing process, the viscosity of the melt controls the diameter of the fibres; residual H_3PO_4 on the pellets could alter the MFI and create thicker fibres [8, p. 144S]. In general, following what is stated in Section 2.2.2, it can be ascertained that H_3PO_4treatment generates deep traps (1.3 eV), but in the case of nonwovens, it also modifies the pre-extrusion morphology. Furthermore, the altered cavity geometry may also influence the local field distribution and the conditions for dielectric barrier discharges, although the dominant charging mechanism in this work is direct corona deposition. Larger cavities would require a higher field to reach the Paschen threshold, potentially reducing the contribution of any cavity-internal DBD to the overall charging process [45, pp. 011101-5, 011101-12-13].

Considering the results presented in **Section 4.3**, **Figure 4.7** shows that the morphology of the fibres of H_3PO_4-treated PP nonwovens is significantly different from that of as-received PP nonwovens, with the former being statistically thicker than the latter. This means that fewer cavities are created, reducing the overall void density available for charge trapping. The altered

cavity geometry may also affect the local field distribution during corona charging, contributing to the lower charge density observed in the treated material. Furthermore, **Table 4.2** shows that the Young's modulus of H_3PO_4-treated PP nonwovens is higher than that of as-received PP nonwovens, providing further evidence for the interpretations outlined above. This dual effect of H_3PO_4—generating deep traps while simultaneously altering morphology —was also documented by Rychkov et al. for melt-blown PP nonwovens [14, p. 560].

Finally, a critical point to highlight, which will be explored in greater depth in **Section 5.2.1**, concerns the fact that chemical treatment with H_3PO_4 structurally modifies PP nonwovens, reducing d_{33} regardless of thermal stability. This is the opposite of what was shown by Rychkov [15, p. 124105-3] for LDPE, where H_3PO_4 increased d_{33} (from ~30 pC/N to ~45 pC/N). However, this is because in LDPE the cavities are pre-formed by template-based lamination before treatment, and although SEM reveals the formation of nanoscale island-like structures on the treated surface [15, pp. 124105-1, 124105-3], the macroscopic cavity geometry—which governs the piezoelectric response—remains unchanged.

Inter-sample variability. Another point to address regarding **Table 4.1** is the range of values assumed by d_{33} in all the configurations considered (e.g. P–; N0; V2: 25–88 pC/N). This phenomenon can be explained by considering the melt-blowing mechanism described in **Section 2.1.2**, which explains how the CV of the fibre diameter distribution in melt-blowing exhibits significant variability, influenced by factors such as air turbulence and die-to-collector distance [8, pp. 148S, 155S]: the structure of the nonwoven fabric is stochastic—as can also be seen in **Figure 4.7**—thus generating great morphological variability between individual samples. By contrast, the controlled geometry achievable through 3D printing yields more reproducible d_{33} values [23, p. 1668].

5.1.2 Interpretation of TSCD and thermal d_{33} decay

Thermally stimulated surface-potential (charge) decay (TSCD). The reference point for this section is **Figure 4.5**, which shows how the surface potential (and consequently also the electrical charge captured in the cavities) of PP nonwovens decreases as the temperature increases. The reason for these decreases is consistent and easily explained if we consider the physical phenomena that occur during TSCD.

The first is Schottky (thermionic) emission (**Section 2.2.1**, **Eq. 2.1**), from which it can be deduced that the current density transmitted through PP nonwovens increases linearly and

exponentially with temperature, resulting in a progressive release of trapped charges and therefore a decay of the surface potential.

The second physical phenomenon to be taken into consideration is Poole-Frenkel emission (**Section 2.2.2**, **Eq. 2.3**). Although it has less significance in the context of TSCD than Schottky emission, this phenomenon helps us understand how, in the bulk, the thermal release of charge carriers from traps follows the same principle seen above: if the thermal energy is sufficiently high, then the energy of the traps is exceeded, and the charge carriers are de-trapped.

Hopping conduction (**Section 2.2.2**, **Eq. 2.5**) is also useful for understanding the TSCD test, as this principle explains how the thermal activation of quantum hopping contributes to the transport of released charges towards the electrodes.

Furthermore, it should be noted that there is an asymmetry between the TSCD curves for positive charges and those for negative charges, i.e. the latter are thermally more stable than the former. This is consistent with the experimental results obtained by Rychkov on LDPE charged at ± 500 V, which show that the TSCD test tends to be more stable for negatively charged materials [15, p. 124105-2]. A similar asymmetry has been reported for FEP ferroelectrets [16, pp. 174105-1, 174105-2].

The better thermal stability is also what characterises the curves defined for H_3PO_4-treated PP nonwovens compared to those obtained for as-received PP nonwovens, and this is consistent with Rychkov's experimental results obtained using TSCD on PP nonwovens charged at –2 kV, where it has been found that chemical treatment with orthophosphoric acid shifts the energy spectrum of the traps, ensuring that charges are released at higher temperatures and therefore a slower decay of the surface potential. [14, pp. 558–560].

Finally, for TSCD performed on H_3PO_4-treated PP nonwovens, the experimental results show a $T_{50\%}$~60 °C and a shift onset of 20–30 °C compared to as-received PP nonwovens, which is consistent with a lower proportion of treated pellets in the blend (30 wt% treated at 100 °C for 24 h) compared to that used by Rychkov for PP nonwovens (86 wt% treated at 110 °C for 24 h, shift onset of 40 °C compared to as-received PP nonwovens) [14, pp. 558–559]. A comparable shift of approximately 21 °C was also observed by Wang et al. [46, p. 79] under significantly more aggressive treatment conditions (85%, 120 °C, 30 min), suggesting that the dose–response relationship may saturate.

Temperature dependence of d_{33}. Figure 4.6 demonstrates that there are consistency and cross-validation between the results obtained for the temperature dependence of d_{33} and the TSCD. If electro-thermal performances are obtained for a single layer, then they apply to the

entire stack. In addition, the results obtained for the temperature dependence of d_{33} show a substantial difference between relative and absolute stability for H_3PO_4-treated and as-received PP nonwovens. In particular, it can be seen that $d_{33,60\,°C} \approx 18\%\, d_{33,20\,°C}$ $(4.2\ pC/N)$ for the H_3PO_4-treated, while for the as-received, we have $d_{33,60\,°C} \approx 14\%\, d_{33,20\,°C}$ $(49\ pC/N)$. What can therefore be deduced is that H_3PO_4-treated PP nonwovens are more stable than as-received PP nonwovens in relative, not absolute, terms. However, both tests amply demonstrate the better electro-thermal stability of H_3PO_4-treated PP nonwovens.

Referring to the theoretical section and the results obtained for TSCD, it is important to remember the charge release mechanisms described in **Sections 2.2.1** and **2.2.2** and the fact that d_{33} depends greatly on the trapped charge; as the charges are released thermally, d_{33} decays proportionally.

The observations made by Assagra regarding 3D-printed PP films should not be underestimated, as they show that the trapped charges, and consequently the piezoelectric coefficient, begin to decrease at temperatures below 60 °C [23, p. 1671].

5.1.3 Role of morphology and mechanical compliance

Fibre morphology and its impact on piezoelectric response. Analysing **Figure 4.7**, the hypotheses expressed in **Section 5.1.1** regarding fibre size (and therefore cavity size) and how these are distributed and influence the charging conditions and d_{33} were well-founded.

In fact, **Section 2.3.2** describes two phenomena that create a correlation between morphology and electrical performance. The melt-blown layer, with its fine-fibre, highly porous microstructure, provides an intrinsic network of gas-filled voids. In addition, the cavity dimensions may influence the local field enhancement during corona charging, and in cases where dielectric barrier discharges occur, Paschen's law links the breakdown trigger voltage to the product of pressure and gap distance [45, p. 011101-5] [22, p. 4]. However, since the samples were charged directly in corona, the role of cavity-internal DBD in the present work remains a secondary consideration.

Delving deeper into the phenomenon through theory, **Section 2.1.2** mentions how thicker fibres generate less concentration of the same, resulting in larger and more variable cavities on average.

Therefore, observations under the microscope confirm the significant impact of the morphology of PP nonwovens on piezoelectric response, consistent with the conclusion of Qiu et al. that morphology is critical for both piezoelectric activity and stability [47, p. 2341009-14].

Mechanical compliance and the electrode effect. Table 4.2 allows us to make a couple of observations regarding mechanical compliance and the effect of the aluminium electrode. We can see that the Young's modulus of H_3PO_4-treated PP nonwovens is always systematically higher than that of as-received PP nonwovens. This implies that the former types of samples are systematically stiffer when subjected to dynamic mechanical stress (such as that provided by the mini shaker) than the latter, with the substantial consequence that the latter will be systematically more prone to deformation, thus improving the measurable d_{33} value.
However, the surprising effect is given by the presence of the aluminium electrode, which greatly increases the Young's modulus of the H_3PO_4-treated and as-received PP nonwovens compared to their counterpart without electrode. This should not be overlooked, as it can have significant implications, especially considering what can be observed in theory.
In fact, according to what is stated in **Section 2.3.1** regarding the measurement of the piezoelectric coefficient and in **Section 2.3.2** regarding the functioning of ferroelectrets, with the quasi-static method (which is what was used for both DoEs), it is assumed that all the applied force deforms the material, consequently generating an interaction between the macrodipoles present in the cavities, from which the piezoelectric coefficient $d_{33} = \Delta Q/\Delta F$ can be obtained. If the rigid electrodes acted as a mechanical filter (thus absorbing part of the applied force), then this means that the measured d_{33} is lower than that intrinsic to the tested materials and has therefore been underestimated. The influence of mechanical loading conditions on the measured d_{33} has also been discussed by Assagra et al. [23, pp. 1668, 1671].

5.2 Comparison with existing literature

Now that the physical mechanisms behind the results observed in **Chapter 4** have been understood, there's going to be a comparison between this research outcomes and the existing literature in terms of d_{33} values measured at room-temperature (**Section 5.2.**1) and the thermal stability of untreated/treated systems (**Section 5.2.2**). The outcome of this comparison and the observations made in **Section 5.1** will lead to the definition of the strengths and limitations of the research outcomes (presented in **Sections 5.3** and **5.4**, respectively).

5.2.1 Comparison of d_{33} values with PP ferroelectrets (film, 3D-printed, nonwoven)

Comparative table. Table 5.1 summarizes the material properties and room-temperature d_{33} values from this work and from the existing literature.

Table 5.1 *Material properties and room-temperature piezoelectric coefficient d_{33} for ferroelectret and piezoelectric polymer systems reported in the literature. The "This work" row refers to melt-blown PP nonwoven stacks corona-charged at ±5 kV (grid voltage), with and without prior H_3PO_4-treated pellets (30 wt% treated blend, pellet treatment at 100 °C, 24 h). N/R = not reported; N/A = not applicable. Values marked with "~" are approximate readings from published figures.*

Ref.	First Author	Year	Material	Morphology	Chemical Treatment	d_{33} RT (pC/N) Treated	d_{33} RT (pC/N) Untreated
This work	Rocchetti	2026	Melt-blown PP (50/50 PP-A/PP-B)	Nonwoven (fibres)	H_3PO_4 30 wt% 24 h, 100 °C	~30	~108–130
[12]	Altafim	2021	FEP laminate + magnetic layer	Laminate (tubular)	None (ferrite layer)	N/A	1120 (magn.) 230 (base)
[14]	Rychkov	2024	Melt-blown PP fibres	Nonwoven (fibres)	H_3PO_4 86% 24 h, 110 °C	N/R (TSCD only)	N/R (TSCD only)
[15]	Rychkov	2012	LDPE ferroelectret	Laminate (tubular)	H_3PO_4 immersion 24 h, 60 °C	~45	~30
[16]	Rychkov	2018	FEP ferroelectret	Laminate (tubular)	$TiCl_4$ vapor 10 min, 100 °C	~90	~90
[23]	Assagra	2020	3D-printed PP films	3D-printed (triangular)	None	N/A	~200 init. ~130 stab.
[45]	Qiu	2010	Various (PP, FEP, etc.)	Foam/Film /Laminate	N/R (review)	160 (FEP tubular)	~hundreds (PP cellular)
[46]	Wang	2016	PP film	Film	H_3PO_4 85% 30 min, 120 °C	N/R	N/R
[47]	Qiu	2023	PP, PETP, PENP, FEP, COC	Cellular / multi-layer	N/R (review)	PENP: 140 PETP: 476 COC: up to 1000	N/R

Benchmarking of room-temperature d_{33}. The d_{33} measured in this work for as-received PP nonwovens is ~108–130 pC/N. This result, compared with the other d_{33} values for other similar materials described in **Table 5.1**, is

(a) lower than the best cellular PP ferroelectrets, which exhibit coefficients of several hundreds of pC/N [45, p. 011101-2]—for instance, the commercial EMFi® film exceeds 600 pC/N [22,

p. 1]. It should be mentioned that the morphology of the cavities is critical for piezoelectric activity and d_{33} stability. In the nonwoven material analysed, the cavities are extremely irregular compared to an engineered structure; therefore, this explains the gap.

(b) lower than that measured for 3D-printed PP films (~200→130 pC/N stabilised) [23, p. 1671]. Here, manufacturing took place in a single step, with monitoring of the decay of d_{33} at room temperature over the days following the initial measurement—until stabilisation after 20 days. The d_{33} reported in this thesis is measured immediately after charging, without waiting for stabilisation; the stabilised value of Assagra [23, p. 1671] is comparable to that measured in this work, which raises the question of whether it would follow the same decay as 3D-printed PP films.

(c) lower than that detected in FEP laminates, both those with a magnetic enhancement: the channelled ferroelectrets without magnetic layer exhibit ~230 pC/N, while the piezoelectric-magnetic design achieves ~1120 pC/N [12, pp. 241901-2–3], and standard FEP laminates without magnetic layer reach ~90 pC/N [16, p. 174105-2]. It should be noted that the piezoelectric-magnetic design employs a fundamentally different excitation mechanism (magnetic force rather than mechanical stress), which accounts for the significantly higher apparent d_{33} [12, p. 241901-2].

(d) higher than that measured for PVDF (approximately 24–34 pC/N) [48, p. 372]. This places the untreated PP nonwoven 4–6 times above the most widely studied piezoelectric polymer, despite the nonwoven format not being optimised for maximum d_{33}.

(e) lower than other engineered ferroelectrets reported in recent reviews, such as PENP (140 pC/N), PETP (476 pC/N), and COC (up to 1000 pC/N) [47, pp. 2341009-3, 2341009-4, 2341009-9]. These systems benefit from precisely controlled cavity geometries, which the stochastic microstructure of the melt-blown nonwoven cannot replicate.

(f) higher than that measured for ferroelectret LDPE (~30 pC/N) [15, p. 124105-3].

Although the nonwoven format has not been fully optimised, the fact that the as-received PP nonwoven exceeds 100 pC/N is a remarkable result for a scalable and solvent-free fabrication process.

However, when analysing the results obtained with H_3PO_4-treated PP nonwovens and comparing them with other similar materials in **Table 5.1**, the observed d_{33} is:

(a) lower than that measured for ferroelectret LDPE (~45 pC/N) [15, p. 124105-2].

(b) lower than that observed for FEP laminates without a magnetic layer (~90 pC/N) [16, p. 174105-2].

(c) lower than other engineered ferroelectrets, such as PENG (140 pC/N), PETP (476 pC/N) and COC (up to 1000 pC/N) [47, pp. 3–4, 9].
In general, it can be seen that the nonwoven format has not been optimised properly, although it should be noted that detecting d_{33} >100 pC/N is still a remarkable result for the type of sample used in DoE 2—which, due to the way it was designed and assembled, is perfectly scalable.

Opposite effect of H_3PO_4 on d_{33}: LDPE vs PP nonwoven. The effect of H_3PO_4 on PP nonwovens and the relative d_{33} measured needs to be compared with a material that has undergone a chemical treatment with H_3PO_4 for 24 h, although at a higher temperature (100 °C vs. 60 °C for LDPE). For this material, treatment with H_3PO_4 increases d_{33} by 50% (from ~30 pC/N to ~45 pC/N) [15, p. 124105-3], while in this work it is observed that treatment with H_3PO_4 decreases it by 70% (from ~108–130 pC/N to ~30 pC/N). A possible explanation for this significant deterioration can be found in the different morphology of the two materials and in the different approaches to the use of H_3PO_4.
It should be noted that in LDPE, the cavities are preformed, which means that the treatment only modifies the surface properties, creating deeper traps without altering the geometry and improving d_{33}. For the PP nonwovens addressed in this work, however, the chemical treatment takes place before extrusion, with the result that the internal geometry of the material is altered and thicker fibres and cavities of different sizes are created. What is therefore noticeable is that the negative morphological effect dominates over the positive effect given by the possible creation of deeper traps. It is therefore important to carry out the same tests but on chemically treated nonwovens after their formation, as was done by Rychkov [14].

Comparison with 3D-printed PP films. Returning to the point made earlier about temporal decay, the d_{33} obtained in this work for as-received PP nonwovens is comparable to the stabilised value measured for 3D-printed PP films (~200→130 pC/N stabilised) [23, p. 1671], but it is not known whether it would decay further over time. This point will be clearly expressed in the analysis of limitations (**Section 5.4**) and future work (**Section 5.5**).

5.2.2 Comparison of thermal stability with treated/untreated systems (PP, LDPE, FEP)

Comparative table. Table 5.2 compares the thermal stability indicator from this work and from the existing literature.

Table 5.2 *Thermal stability indicators and key findings for the systems listed in Table 5.1a. T_{50}% = temperature at which the measured quantity drops to 50% of its initial value; SP = surface potential; init. = initial value; tr. = treated; untr. = untreated; est. = estimated.*

Ref.	First Author	d_{33} at 60 °C	d_{33} at 100 °C	$T_{50\%}$ (d_{33})	Trap Energy (eV)	$T_{50\%}$ (SP) Treated	$T_{50\%}$ (SP) Untreated	Key Finding
This work	Rocchetti	P−: 38% init. P+: 14% init.	P−: <2% P+: 6%	P−: ~45 °C P+: ~35 °C	N/R	P+: ~80–90 °C (est.)	P−: ~60–70 °C (est.)	High init. d_{33}; limited thermal stability; H_3PO_4 improves relative stability but lowers absolute d_{33}
[12]	Altafim	N/R	N/R	N/R	N/R	N/R	N/R	Magnetic enhancement; not directly comparable
[14]	Rychkov	N/R	N/R	N/R	~1.3	~165 °C	~140 °C	Deep traps at 1.3 eV; different treatment conditions
[15]	Rychkov	N/R	N/R	~90 °C (tr.) ~50 °C (untr.)	N/R	~140 °C	~80 °C	d_{33} shift 40 K; TSCD shift 60 K; closest conditions to this work
[16]	Rychkov	~90% init. (treated)	N/R	~180 °C (tr.) ~130 °C (untr.)	N/R	~190 °C (tr. positive)	N/R	Best thermal stability; $TiCl_4$ stabilizes positive charges; 30% residual at 200 °C
[23]	Assagra	~190 pC/N (stable)	~75 pC/N (39%)	~95 °C	N/R	N/R	N/R	One-step fabrication; 40% decay in 20 days then stable
[45]	Qiu	N/R	N/R	N/R	N/R	N/R	N/R	Review; void morphology critical for $\boldsymbol{d_{33}}$
[46]	Wang	N/R	N/R	N/R	Deeper traps (qualitative)	~124 °C	~104 °C	H_3PO_4 improves PP charge stability; T_{50}% shift ~21 °C
[47]	Qiu	PENP: stable to 80 °C	N/R	PENP: >100 °C COC: ~110 °C	N/R	N/R	N/R	Review; morphology critical for activity and stability

Comparison of TSCD curves. From the curves shown in **Figure 4.5** and the information reported in **Table 5.2**, it can be seen that in this work for as-received PP nonwovens, the onset temperature is ~60 °C ($T_{50\%}$), a result consistent with the benchmark for PP, which establishes that the stability of d_{33} (and therefore of the charge trapped in the cavities) decreases significantly at temperatures above 60 °C [22, p. 4].

As for the results obtained for H_3PO_4-treated PP nonwovens, there is a shift onset forward ~20–30 °C, but this result deserves more in-depth discussion and a more accurate comparison with other treatment conditions (ordered by increasing intensity):

(a) for the PP films analysed by Wang [46, pp. 78–80], a treatment with H_3PO_4 at 120 °C for 30 minutes was used to obtain PP films with 85% phosphorus treatment and a shift onset of ~21 °C. In both cases, it can be inferred that the intervention of H_3PO_4 improves charge stability. The chemical treatment conditions were more aggressive than those used in this study (85% vs. 30%, 120 °C vs. 100 °C), but the shift onset is comparable (~21 °C vs. ~20–30 °C). This suggests a saturating effect: above a certain concentration/temperature threshold, the shift does not increase proportionally. Alternatively, the difference in format (film vs. nonwoven) could mask the dose-response effect.

(b) for the ferroelectrets LDFEs treated by Rychkov [15, pp. 1–2], it was used a chemical treatment with H_3PO_4 for 24 h, although at a higher temperature (100 °C vs 60 °C for LDPE), but in this case by immersing the post-extrusion LDPE in H_3PO_4, obtaining a shift of 60 °C, which is much greater than the shift obtained in this work (despite similar conditions). In this case, the use of a specific base material (PP vs. LDPE) and the timing of the chemical treatment (pre-extrusion vs. post-extrusion) play a key role in the response to the treatment.

(c) for the melt-blown PP nonwovens analysed by Rychkov [14, pp. 558–559, 561–562], a treatment with H_3PO_4 at 110 °C for 24 h was used to obtain PP films with 86% phosphorus treatment and a shift onset of ~40 °C with deep traps of 1.3 eV. These are the most aggressive treatment conditions among those observed and produce significantly deeper traps and a greater shift; the working conditions observed in this thesis (30 wt%/100 °C) are insufficient to achieve the same level.

To summarise the dose-response effect: H_3PO_4 a 30 wt% blend of H_3PO_4-treated pellets at 100 °C for 24 h is sufficient to achieve an improvement over as-received PP nonwoven, but insufficient to reach the levels achieved by Rychkov with 86 wt% treated pellets at 110 °C [14].

Comparison of d_{33} thermal profiles. Based on the data reported in **Table 5.2**, several comparisons can be drawn between the results of this work and those available in the existing literature:

(a) The 3D-printed PP films exhibit a d_{33} that remains stable up to 60 °C, with a decrease of 17% at 80 °C and 60% at 100 °C [23, p. 1671]. In contrast, the as-received PP nonwovens investigated in this work show a d_{33} reduction of 62% already at 60 °C, significantly worse than that reported in [23].

(b) For LDPE ferroelectrets, $T_{50\%}(d_{33})$ values of approximately 90 °C (treated) and 50 °C (untreated) have been reported, corresponding to a shift of 40 K [15, pp. 124105-1, 124105-2]. Once again, the base material (PP vs. LDPE) and the timing of the chemical treatment (pre-extrusion vs. post-extrusion) play a key role in the response to the treatment.

(c) For FEP ferroelectrets, a markedly superior thermal stability of d_{33} is observed, since $TiCl_4$ stabilises the positive charges. This is evidenced by a residual d_{33} of 30% of the initial value even at 200 °C [16, pp. 174105-2, 174105-3]. This represents an upper benchmark for thermal stability among polymeric ferroelectrets; the gap with the PP nonwoven investigated in this thesis (approximately 45 °C vs. 180 °C for $T_{50\%}(d_{33})$) highlights the significant margin for improvement achievable through both the choice of base material (FEP vs. PP) and the chemical treatment agent ($TiCl_4$ vs. H_3PO_4).

Cross-material perspective. Analysing the thermal stability comparison between ferroelectret PP analysed in **Tables 5.1, 5.2 and 2.3**, the following observations can be made:

(a) regarding d_{33} measured at room temperature, the nonwoven PP analysed in this study has values higher than those measured in PVDF and composite materials, but lower than those measured in cellular PP and laminated FEP.

(b) With regard to thermal stability, the nonwoven PP presented in this work has the worst possible performance, as the d_{33} trend decreases with temperature much faster than in cellular PP (comparable in performance to 3D-printed PP films), laminated FEP and ceramic materials.

A closer examination of the thermal stability comparison between PP ferroelectrets and PVDF reveals that **Table 2.3** juxtaposes two non-equivalent quantities: the onset of charge de-trapping in PP (≈ 60 °C) and the Curie temperature of PVDF (T_C ≈ 100 °C). The latter represents the irreversible ferroelectric phase transition, not the onset of piezoelectric decay. Sherman et al. have shown that under prolonged isotropic convective annealing (≥ 10 min), prepoled PVDF films lose nearly 30 % of their d_{33} at 100 °C, as reported in studies cited by Sherman et al. [25,

p. 5114], with the onset of measurable degradation documented at approximately 70 °C, as reported in earlier work cited by Sherman et al. [25, p. 5111]. Crucially, this degradation was attributed to the thermally activated release of trapped surface charge from destabilised semi-crystalline domains, and X-ray diffraction confirmed that no mesoscopic β→α phase transition occurs at these temperatures [25, p. 5117]. Under shorter exposure (60 s, unidirectional conductive heating), the same authors observed only ≈ 5 % loss at 100 °C [25, p. 5114], demonstrating a strong time dependence of the decay process.

This evidence has two implications for the positioning of the present work. First, the practical thermal stability gap between PP ferroelectrets and PVDF is narrower than **Table 2.3** suggests when the same metric—onset of d_{33} decay under sustained isothermal exposure—is applied to both systems: ≈ 60 °C for PP versus ≈ 70 °C for PVDF. Second, while the microscopic origin of the released charges differs—corona-injected charges trapped on cavity walls in PP ferroelectrets versus compensation charges bound to ferroelectric dipoles in PVDF—the macroscopic phenomenology is analogous: in both cases, thermally activated charge release, rather than a structural phase transition, governs the practical onset of piezoelectric decay. Consequently, the untreated PP nonwoven investigated in this thesis, with a d_{33} of 108–130 pC/N (4–6 × that of PVDF) and a comparable thermal onset of ≈ 60 °C, exhibits a performance-to-stability ratio that is more favourable than the simple T_C-based comparison of **Table 2.3** would imply.

In summary, this work ranks in the middle range among the materials observed, as it has a remarkable d_{33} for a non-optimised format but has limited thermal stability. Notably, H_3PO_4 treatment was found to have the opposite effect on d_{33} in PP nonwovens (−70%) compared to LDPE (+50%), attributed to the pre-extrusion application altering fibre morphology rather than solely modifying surface trap properties. The sensitivity/stability trade-off, identified in the literature as "the central engineering challenge", is confirmed and quantified for the first time in the nonwoven format.

5.3 Strengths of the research outcomes

Novel contribution. An important strength lies in the fact that this is the first truly systematic characterisation (d_{33} + thermal stability) in melt-blown PP nonwoven fabric. Specifically, Rychkov [14, pp. 560–562] had already studied this type of material, but only in depth for TSCD. This thesis also adds the analysis of d_{33} and its dependence on temperature in melt-blown PP nonwovens.

High initial d_{33} for a nonwoven format. Furthermore, the initial value of d_{33} for as-received PP nonwovens is ~108–130 pC/N, which is 4–6 times greater than that measured for PVDF (24–34 pC/N) [48, p. 372]. When compared to EMFi® (>600 pC/N [22]), the nonwoven analysed in this thesis achieves ~20% of the commercial benchmark with a simpler and more scalable format.

Systematic experimental design. A total of 112 measurements (72 DoE 1 + 40 DoE 2) were submitted to obtain the best possible characterisation for melt-blown PP nonwovens. This indicates that the DoEs used during this work are well structured, allowing for consistent multimodal characterisation.

Direct link between processing and performance. It is possible to find an end-to-end connection between the starting point (pellets), the process of creating the material under analysis (melt-blowing), the morphology that is created because of extrusion and chemical treatment, and the resulting electrical properties.

5.4 Limitations and challenges

Absence of a physical/mathematical model. A major drawback is the lack of a predictive model to correlate the cavity geometry of PP nonwovens with the local charging conditions—including possible contributions from dielectric barrier discharges—and the resulting charge trapped in the cavities and the d_{33} generated. A more in-depth study using FEM could have clearly and distinctly shown the mechanical contribution from the electrical one. Rychkov's analysis of PP nonwovens cites Simmons's model for reconstructing trap energy [14, p. 558]; this model could also be extended and adapted to applications related to those presented in this thesis.

Electrode stiffness effect. Another point of departure from the results derived from literature concerns the surface hardness test carried out in **Section 4.3.2**. **Table 4.2** clearly shows that Shore A (and consequently also Young's modulus) became three times greater with the introduction of aluminium electrodes (from ~26–31 to ~72–73), making the d_{33} measured in both DoE 1 and DoE 2 significantly underestimated. A possible solution in the future could be to use more flexible electrodes (conductive silver, conductive fabrics), as well as performing a preliminary interferometric measurement with a laser of the ferroelectret + electrode combination.

Limited statistical robustness. The ANOVA performed on the 72 individual measurements (Section 4.1) confirms that the residual error accounts for 23.2% of the total variation, consistent with the ±60% inter-sample variability observed in certain configurations (e.g., P−; N0; V2 ranges from 25 to 88 pC/N). Despite this scatter, the main effects of P and V remain highly significant ($p < 0.001$), demonstrating that the overall trends are robust even though individual point estimates carry substantial uncertainty. Nevertheless, the modest number of repetitions (n = 3 per configuration) limits the statistical power for detecting smaller interaction effects, and increased replication — comparable to that adopted for DoE 2 — would be needed for more precise estimates of d_{33}.
In addition to this, it should be borne in mind that having a more controlled geometry can make measurements and results more reproducible, as demonstrated by Assagra et al. for 3D-printed PP films [23, p. 1668].

Treatment conditions are not optimized. Based on the results shown in **Tables 5.1** and **5.2** regarding comparisons between types of chemical treatments and their effects on piezoelectric and thermal stability, it can be inferred that there is room for optimisation of the process adopted in this thesis and that used by Rychkov for nonwoven PPs using H_3PO_4 (30 wt% blend, pellets treated at 100 °C vs. 86 wt%, 110 °C [14, p. 558]).
Moreover, this thesis did not compare the change that can be recorded between pre-extrusion and post-formation chemical treatment, since the only type of comparison that could be made was with results already existing in the literature but in relation to the LDPE studied by Rychkov [15, p. 124105-2].

Temporal decay is not characterized at room temperature. In the study conducted on 3D-printed PP films, the decay of d_{33} at room temperature was investigated, finding that it reduces to 40% of its original value in 20 days [23, p. 1671]. This analysis was not carried out for the nonwoven PP covered in this thesis, leaving doubt as to whether such decay is plausible for this type of polymeric ferroelectret material.

5.5 Suggestions for future works

Optimization of the chemical treatment. A first suggestion for future work must necessarily concern the improvement of the chemical treatment used in this study. One possible direction that could be taken is the introduction of a specific DoE to study the effects of H_3PO_4,

considering a comparison between different types of concentration (30–86 wt%), temperature (100–120 °C) and duration (30 min – 24 h).
In addition to this, it would be appropriate to compare pre-extrusion treatment (as was done in this thesis) with post-formation treatment (treating the finished nonwoven), as the latter option could preserve the morphology of the cavities while introducing deep traps.
Finally, the use of $TiCl_4$ as an alternative to H_3PO_4 can be evaluated, following the same treatment used by Rychkov (100 °C, 10 min [16, p. 174105-2]) or defining one from scratch.

Development of a predictive model. As mentioned in **Section 5.4**, a fundamental element missing from this work was the absence of a physical-mathematical model to characterise the piezoelectric performance in relation to the morphology of the treated material (fibre diameter, porosity) and the loading conditions.
One suggestion in this direction would be to create two FEMs, one to study the deformation of the cavities caused by chemical treatment and another to analyse the role of cavity geometry on the local field distribution and charge deposition efficiency, including any contribution from dielectric barrier discharges.
A starting point would be the Simmons framework cited by Rychkov [14, p. 557], to see if it is adaptable or not to the material under study.

Long-term stability characterization. This study examined the short-term thermal stability of d_{33} for PP nonwovens through isothermal testing. However, it did not analyse how PP nonwovens behave in terms of piezoelectric performance in the long term, as was done by Assagra, who analysed the decay of d_{33} at room temperature for entire weeks/months and found a 40% decay in 20 days and subsequent stabilisation [23, p. 1671].
Consequently, this could be a possible direction for future experiments on PP nonwovens, subjecting them—in addition to decay at room temperature—to repeated thermal cycles and analysis of the effect of humidity (relevant for wearable applications of PP nonwovens).

Toward energy harvesting applications. Referring to **Section 1.1** on possible existing applications for piezoelectric materials (in particular, PVDF), it is worth mentioning some case studies of possible practical applications in which PP nonwovens could be of great importance: **(a)** with reference to Sarker's study on micro-energy harvesting for IoT platforms, the plausible power ranges go from 10 nW for standby applications to 100 W for desktop computer operation, including hearing aid applications that require power supports in the order of 100 μW [49, p.

8]. The nonwoven PP analysed in this work with d_{33} > 100 pC/N at room temperature could power very low-power IoT sensors, such as those mentioned above.

(b) With regard to the flexible harvesters analysed by Almarri, very low-power applications should be mentioned here, such as 8.4 W shoe devices and wireless data transfer systems that operate on 30 μW of power [50, pp. 3, 5]. With a view to meeting the need for flexible materials for low-frequency movements, PP nonwoven is a good practical solution, as it is intrinsically flexible.

All these applications analyse fibre-based harvesters based on electrospun PVDF, whose performance can be matched or even surpassed by a more scalable and solvent-free alternative such as melt-blown PP nonwovens. Furthermore, the fact that it has a performance limit for its piezoelectric properties at ~60 °C makes it compatible with wearable applications on humans (who have a body temperature of ~37 °C).

Consequently, a possible future direction could be the creation of a demonstrator prototype for EH applications based on PP nonwovens, with an attached measurement of the electrical power that can be generated from it under periodic mechanical stress.

6. CONCLUSIONS

The experimental programme outlined in **Section 1.3** was systematically addressed through two complementary Designs of Experiments. Melt-blown PP nonwoven mats were produced from both untreated and blends containing 30 wt% of H_3PO_4-treated pellets (Activity 1), corona-charged and characterised for d_{33} as a function of temperature (Activity 2), subjected to TSCD measurements to map charge stability (Activity 3), and the treated/untreated results were directly compared (Activity 4). A full factorial ANOVA on the 72 individual d_{33} measurements of DoE 1 confirmed that the phosphorus treatment is the single most influential factor (43.7% of total variation, $F = 90.4$, $p < 0.001$), followed by the charging voltage (13.9%, $F = 14.4$, $p < 0.001$) and the number of intermediate layers (5.8%, $F = 4.0$, $p = 0.013$). A significant P × V interaction ($p = 0.039$) indicates that the voltage effect differs between treated and untreated samples. While the H_3PO_4 treatment was initially expected to simultaneously improve both piezoelectric performance and thermal stability, the experimental evidence revealed a more nuanced picture. The DoEs show that as-received PP nonwovens exhibit a d_{33} approximately 3–4 times higher than their H_3PO_4-treated counterparts (~108–130 pC/N vs. ~30 pC/N), while the treated samples demonstrate improved relative thermal stability. This outcome indicates that H_3PO_4 treatment applied before extrusion does not yield the expected improvement in absolute piezoelectric performance; instead, the morphological alterations induced by the treatment—thicker fibres, larger and fewer cavities—dominate over the beneficial effect of deeper charge traps, resulting in a net decrease of d_{33}.

It is therefore necessary to note that, an alternative way of using chemical additives on PP nonwovens will have to be developed to ensure truly better thermal stability at high temperatures and the creation of deeper traps. It will also be necessary to verify how piezoelectric phenomena can be improved/worsened if the chemical treatment takes place before or after the extrusion or formation of the material. Furthermore, an ad hoc mathematical model to avoid unexpected responses and study how morphology could influence the piezoelectric response will be necessary, given that this work lacked one. This could also be useful in terms of extending the size of the tested sample to larger formats, while maintaining the structure of two layers charged with opposite voltages and electrically neutral intermediate layers. This format was very useful because it greatly contributed to measuring d_{33} values well above the PVDF reference benchmark (~20–30 pC/N).

However, it is worth noting that the d_{33} values measured in this thesis were significantly underestimated due to the fact that aluminium electrodes were used, which were a simple

functional solution to the need to use an electrode to be applied to the polymer ferroelectret, but potentially absorbed part of the force applied during the experiments, from which a potentially underestimated value of d_{33} was measured. A practical future solution in this regard will require the use of more flexible conductive materials.

In summary, it is still important to mention that this work ranks in the middle range among the ferroelectret polymers observable in literature, as it has a remarkable d_{33} for a non-optimised format but has limited thermal stability. Notably, H_3PO_4 treatment was found to have the opposite effect on d_{33} in PP nonwovens (−70%) compared to LDPE (+50%), attributed to the pre-extrusion application altering fibre morphology rather than solely modifying surface trap properties. The sensitivity/stability trade-off, identified in the literature as "the central engineering challenge", is confirmed and quantified for the first time in the nonwoven format.

7. REFERENCES

[1] Smith M. and Kar-Narayan S., "Piezoelectric polymers: theory, challenges and opportunities", *International Materials Reviews*, vol. 67, no. 1, pp. 65–88, 2022. doi: 10.1080/09506608.2021.1915935.

[2] Liu L. et al., "Recent Progress in the Energy Harvesting Technology—From Self-Powered Sensors to Self-Sustained IoT, and New Applications", *Nanomaterials*, vol. 11, art. 2975, 2021. doi: 10.3390/nano11112975.

[3] Wu Y. et al., "Piezoelectric materials for flexible and wearable electronics: A review", *Materials & Design*, vol. 211, art. 110164, 2021. doi: 10.1016/j.matdes.2021.110164.

[4] Ali A. et al., "Recent advances in piezoelectric wearable energy harvesting based on human motion: Materials, design, and applications", *Energy Strategy Reviews*, vol. 53, art. 101422, 2024. doi: 10.1016/j.esr.2024.101422.

[5] Ebewele R. O., *Polymer Science and Technology*, CRC Press, Boca Raton, New York, 2000.

[6] Haque S. K. M. et al., "Application and Suitability of Polymeric Materials as Insulators in Electrical Equipment", *Energies*, vol. 14, no. 10, art. 2758, 2021. doi: 10.3390/en14102758.

[7] Zhang L. et al., "Crystalline Modification and Its Effects on Dielectric Breakdown Strength and Space Charge Behaviour in Isotactic Polypropylene", *Polymers*, vol. 10, no. 4, art. 406, 2018. doi: 10.3390/polym10040406.

[8] Kara Y. and Molnár K., "A review of processing strategies to generate melt-blown nano/microfiber mats for high-efficiency filtration applications", *Journal of Industrial Textiles*, vol. 51, no. 1S, pp. 137S–180S, 2022. doi: 10.1177/15280837211019488.

[9] Song J. et al., "Continuous production and properties of multi-level nanofiber air filters by blow spinning", *RSC Advances*, vol. 10, pp. 19615–19620, 2020. doi: 10.1039/D0RA01656J.

[10] Goh G. D. et al., "Large-format additive manufacturing of polymers: a review of fabrication processes, materials, and design", *Virtual and Physical Prototyping*, vol. 19, no. 1, art. e2336160, 2024. doi: 10.1080/17452759.2024.2336160.

[11] Calisir M. et al., "Clogging performance of micro/nanofibrous laminated composite air filter media", *Journal of Industrial Textiles*, vol. 52, pp. 1–16, 2022. doi: 10.1177/15280837221113084.

[12] Altafim R. A. P. et al., "Piezoelectric-magnetic behaviour of ferroelectrets coated with magnetic layer", *Applied Physics Letters*, vol. 119, art. 241901, 2021. doi: 10.1063/5.0071231.

[13] Chiu F.-C., "A Review on Conduction Mechanisms in Dielectric Films", *Advances in Materials Science and Engineering*, vol. 2014, art. 578168, 2014. doi: 10.1155/2014/578168.

[14] Rychkov D. et al., "Electret Charge Stability in Melt-blown Polypropylene Fibers", in *2024 IEEE Conference on Electrical Insulation and Dielectric Phenomena (CEIDP)*, 2024. doi: 10.1109/CEIDP61745.2024.10907715.
[15] Rychkov D. et al., "Treatment with orthophosphoric acid enhances the thermal stability of the piezoelectricity in low-density polyethylene ferroelectrets", *Journal of Applied Physics*, vol. 111, art. 124105, 2012. doi: 10.1063/1.4729866.
[16] Rychkov D. and Altafim R. A. P., "Template-based fluoroethylenepropylene ferroelectrets with enhanced thermal stability of piezoelectricity", *Journal of Applied Physics*, vol. 124, art. 174105, 2018. doi: 10.1063/1.5041374.
[17] Li J. F., "Fundamentals of Piezoelectricity", *Lead-Free Piezoelectric Materials*, Wiley-VCH, pp. 1–18, 2021.
[18] IEEE, "IEEE Standard on Piezoelectricity", *ANSI/IEEE Std 176-1987*, pp. 1–74, 1988. doi: 10.1109/IEEESTD.1988.79638.
[19] Ali M. et al., "Biodegradable Piezoelectric Polymers: Recent Advancements in Materials and Applications", *Advanced Healthcare Materials*, vol. 12, art. 2300318, 2023. doi: 10.1002/adhm.202300318.
[20] Kawai H., "The piezoelectricity of poly(vinylidene fluoride)", *Japanese Journal of Applied Physics*, vol. 8, pp. 975–976, 1969. doi: 10.1143/JJAP.8.975.
[21] Pîrvu C. I. et al., "Participation of Polymer Materials in the Structure of Piezoelectric Composites", *Polymers*, vol. 16, art. 3603, 2024. doi: 10.3390/polym16243603.
[22] Moreira M. M. A. C. et al., "Piezoelectrets: a brief introduction", *IEEE Sensors Journal*, vol. 21, no. 20, art. 22317, 2021. doi: 10.1109/JSEN.2021.3096424.
[23] Assagra Y. A. O. et al., "A New Route to Piezo-Polymer Transducers: 3D Printing of Polypropylene Ferroelectrets", *IEEE Transactions on Dielectrics and Electrical Insulation*, vol. 27, no. 5, pp. 1668–1674, 2020. doi: 10.1109/TDEI.2020.008461.
[24] Shaukat H. et al., "A Review of the Recent Advances in Piezoelectric Materials, Energy Harvester Structures, and Their Applications in Analytical Chemistry", *Applied Sciences*, vol. 13, art. 1300, 2023. doi: 10.3390/app13031300.
[25] Sherman J. D., Elloian J., Jadwiszczak J. and Shepard K. L., "On the temperature dependence of the piezoelectric response of prepoled poly(vinylidene fluoride) films", ACS Applied Polymer Materials, vol. 2, no. 11, pp. 5110–5120, 2020. doi: 10.1021/acsapm.0c00902.
[26] FuG Elektronik GmbH, "Bipolar high voltage power supplies—Series HCB (Design example HCB 7-6500)" and "High voltage power supplies—Series HCP (Design example HCP

35-35000)", Product overview / catalogue, ver. V 0112, Schechen (Germany), n.d., pp. 19–20, 41–42.
[27] Conrad Electronic, "VOLTCRAFT FG-30802T Function generator 1 µHz–80 MHz, 2-channel (product page)", n.d. [Online]. Available: https://www.conrad.com/en/p/voltcraft-fg-30802t-function-generator-1-hz-80-mhz-2-channel-arbitrary-noise-pulse-rectangle-sinus-triangle-manu-2139575.html. Accessed: 02/01/2026.
[28] Brüel & Kjær, "Power Amplifier Type 2718", Product Data BP 1928–14, Hottinger Brüel & Kjær A/S, Jun. 2021, pp. 1–2.
[29] Brüel & Kjær Sound & Vibration Measurement A/S, "NEXUS Conditioning Amplifier for Very High Input Types 2692-C and 2692-D", Product Data BP 1976–13, Mar. 2015, pp. 1–4.
[30] Hottinger Brüel & Kjær A/S, "Modal and Measurement Exciters—Mini-shaker Type 4810", Product Data BP 0232–16, Jun. 2021, pp. 1–2.
[31] Brüel & Kjær, "Force Transducer—DeltaTron® Force Transducers Types 8230, 8230-001, 8230-002 and 8230-003", Product Data BP 2080–11, May 2001, pp. 1–2.
[32] Tektronix, "3 Series MDO Mixed Domain Oscilloscopes Datasheet", document no. 48W-61535-10, Aug. 2025, pp. 1–35.
[33] Trek, Inc., "Trek Model 341B High-Speed, High-Voltage Electrostatic Voltmeter", Sales datasheet / brochure, 2014, pp. 1–2.
[34] OMEGA Engineering, "Introduction to Temperature Controllers", Technical handbook excerpt, n.d., pp. 2–5.
[35] DwyerOmega, "Introduction to Pt100 RTD Temperature Sensors (RTD Hub)", n.d. [Online]. Available: https://www.dwyeromega.com/en-us/resources/rtd-hub. Accessed: 03/01/2026.
[36] Lagerwerk GmbH, "G. MAIER R12/SSR/PT100/3300/230, Temperature regulator 3.3 kW (Model: R12SSRPT1003300230)", n.d. [Online]. Available: https://www.lagerwerk.com/en/electrics-mechanics/automation-devices/others/23598/g.-maier-r12/ssr/pt100/3300/230-temperature-regulator-3-3kw. Accessed: 03/01/2026.
[37] burster präzisionsmesstechnik gmbh & co kg, "Tension Compression Load Cell—Model 8435", Product Data, document no. 4298-008435EN-5699-101532, n.d., pp. 1–2.
[38] Heckert N. A., Filliben J. J., Croarkin C. M., Hembree B., Guthrie W. F., Tobias P. and Prinz J., "NIST/SEMATECH e-Handbook of Statistical Methods", NIST Handbook 151, National Institute of Standards and Technology, Gaithersburg (MD), 2002 [Online]. Available: https://www.itl.nist.gov/div898/handbook/. Accessed: 12/03/2026.

[39] ISO 19069-1:2015, Plastics—Polypropylene (PP) moulding and extrusion materials—Part 1: Designation system and basis for specifications, International Organization for Standardization, Geneva, 2015.
[40] KEYENCE, "VHX-5000 Digital Microscope", Data Sheet, KEYENCE America, Feb. 2026, pp. 1–2.
[41] Heinrich Bareiss Prüfgerätebau GmbH, "DIGI TEST II—Shore/IRHD durometer", Product brochure / datasheet, Oberdischingen (Germany), n.d., pp. 3–4, 17–19.
[42] Harry Gestigkeit GmbH, "PRÄZITHERM—High temperature hot plate of titanium up to 600 °C (PZ 28-3T / PZ 28-3TD) with PID temperature controller (TR 28-3T) or programmer (PR 5-3T)", Technical Datasheet TI 09, Düsseldorf (Germany), n.d., pp. 1–2.
[43] Makeblock Co., Ltd., "LaserBox User Manual", Document IDs D1.3.5_KD010121000 / D1.3.5_KD010098000, Shenzhen, Guangdong Province, China, n.d., pp. 1–20.
[44] Mix A. W. and Giacomin A. J., "Standardized Polymer Durometry", *Journal of Testing and Evaluation*, vol. 39, no. 4, pp. 696–705, 2011. doi: 10.1520/JTE103205.
[45] Qiu X., "Patterned piezo-, pyro-, and ferroelectricity in poled polymer electrets", *Journal of Applied Physics*, vol. 108, art. 011101, 2010. doi: 10.1063/1.3457141.
[46] Wang J., Rychkov D. and Gerhard R., “Influence of Surface Modifications with Orthophosphoric Acid on the Charge Stability of Polypropylene Electrets”, *2016 IEEE Conference on Electrical Insulation and Dielectric Phenomena (CEIDP)*, pp. 78–80, 2016. doi: 10.1109/CEIDP.2016.7785496.
[47] Qiu X. et al., "Ferroelectrets: Heterogenous polymer electrets with high piezoelectric sensitivity for transducers", *Journal of Advanced Dielectrics*, vol. 13, art. 2341009, 2023. doi: 10.1142/S2010135X23410096.
[48] Mohammadpourfazeli S. et al., "Future prospects and recent developments of polyvinylidene fluoride (PVDF) piezoelectric polymer; fabrication methods, structure, and electro-mechanical properties", *RSC Advances*, vol. 13, pp. 370–387, 2023. doi: 10.1039/d2ra06774a.
[49] Sarker M. R. et al., "Micro energy harvesting for IoT platform: Review analysis toward future research opportunities", *Heliyon*, vol. 10, art. e27778, 2024. doi: 10.1016/j.heliyon. 2024.e27778.
[50] Almarri N. et al., "Piezoelectric energy harvesting and ultra-low-power management circuits for medical devices", *Nano Energy*, vol. 131, art. 110196, 2024. doi: 10.1016/j.nanoen.2024.110196.